

The authors would like to thank the reviewer for their insightful comments. A point by point response to the reviewer's comments, along with changes made to the manuscript as a result, are included below.

**R1. The advantage of basing forward calculations on empirical relationships, as opposed to fundamental radiative transfer and scattering theory, is not well established in the manuscript. One justification for the approach in the paper is that using empirical relationships means that one does not need to make assumptions about scatterers (e.g., a spherical assumption), but this simply exchanges a known assumption with an assumption (or set of assumptions) hidden in the empirical relationships. And most of these empirical relationships are actually retrievals, just inverted! If we're going to do forward calculations based on retrievals, we might as well just use the retrievals on the observations and cast all the quantities in terms of geophysical variables, which are easier to interpret. This approach seems like a big step back compared to performing fundamental radiative transfer/scattering calculations on the model fields, which yields an independent forward calculation of the observational fields. Furthermore, the assumptions in the empirical relationships may not be consistent with the assumptions in the model cloud microphysical parameterization (e.g., the assumed distributions). Consistent forward calculations of model variables should use assumptions consistent with the cloud-physics scheme in the model.**

A1. In response to this comment by the reviewer we now elaborate within the manuscript on the reasoning behind our approach:

“Hydrometeor properties that impact backscattering include size, phase, composition, geometrical shape, orientation and bulk density. Were plausible representations for these hydrometeor properties available as part of the model formulation, fundamental radiative scattering transfer calculations would be the most accurate way to transform model hydrometeor properties to observables. However, in most GCMs such detailed hydrometeor information is highly simplified (e.g., fixed particle size distribution shapes) or not explicitly represented (e.g., orientation and realistic geometrical shape), complicating the process of performing direct radiative scattering transfer calculations. Chepfer et al. (2008) proposed an approach by which lidar backscattered power can be forward-simulated using model output hydrometeor effective radius. Their approach, based on Mie theory, relies on the assumption that cloud particles (both liquid and ice) are spherical and requires additional assumptions about hydrometeor size distributions and scattering efficiencies. Similarly, the COSP (Bodas-Salcedo et al., 2011) and ARM Cloud Radar Simulator for GCMs (Zhang et al., 2017) packages both use QuickBeam for the estimation of radar backscattered power (i.e., radar reflectivity; Haynes et al., 2007). QuickBeam computes radar reflectivity using Mie theory again under the assumption that all hydrometeor species are spherical and by making additional assumptions about the shape of hydrometeor size distributions as well as mass-size and diameter-density relationships. While some of these assumptions may be consistent with the assumptions in model cloud microphysical parameterizations, some are not adequately realistic (e.g., spherical ice) or complete for accurate backscattering estimation and it is typically very difficult to establish the sensitivity of results to all such assumptions.

To avoid having to make ad hoc assumptions about hydrometeor shapes, orientations, and compositions, which are properties that also remain poorly documented in nature, (GO)<sup>2</sup>-SIM

employs empirical relationships to convert model output to observables. These empirical relationships based on observations, direct or retrieved with their own sets of underlying assumptions, are expected to capture at least part of the natural variability in hydrometeor properties. Additionally empirical relationships are computationally less expensive to implement than direct radiative scattering calculations, thus enabling the estimation of an ensemble of backscattering calculations using a range of assumptions in an effort to quantify part of the backscattering uncertainty (see Sec. 7). The empirical relationships proposed require few model inputs, potentially enhancing consistency in applying (GO)<sup>2</sup>-SIM to models with differing microphysics scheme assumptions and complexity. Section 6 will show that, while the empirical relationships employed in (GO)<sup>2</sup>-SIM may not be as exact as direct radiative scattering calculations, they produce backscattering estimates of sufficient accuracy for hydrometeor phase classification, which is the main purpose of (GO)<sup>2</sup>-SIM at this time.”

**R2. The manuscript advocates a phase determination that is solely in forward-calculation space and fairly well articulates the reason for this. However, this approach does not take advantage of knowing the actual hydrometeor fields, and therefore this discards a great deal of potentially useful information. Is there any way the approach in the manuscript can take some advantage of the fields in hydrometeor (model) space?**

A2. As articulated in the manuscript our goal is “[...] development of a phase classification algorithm that can be applied to observables, forward-simulated and real.” This explains why we avoided developing a hydrometeor-phase classifier dependent on model output quantities that are not accessible via observations. Rather, we take advantage of the fields in model space by using them to 1) evaluate the ability of Doppler velocity and Doppler spectral width observations to be used for hydrometeor phase classification (a concept which was developed empirically and was not formally evaluated) and to 2) select optimum classification thresholds to minimize false detection in model space.

This reasoning is expressed in the following modified manuscript excerpts:

“While the thresholds used for the radar reflectivity, lidar backscattered power, and lidar depolarization ratio are generally accepted by the remote sensing community, the same cannot be said about the radar Doppler velocity and Doppler spectral width thresholds suggested by Shupe (2007). Because simulated mixing ratios of liquid and ice hydrometeors are known in the (GO)<sup>2</sup>-SIM framework, the use and choice of all such thresholds for phase classification can be evaluated using joint frequency of occurrence histograms of hydrometeor mixing ratios for a single species and forward-simulated observable values (resulting from all hydrometeor types; Fig. 6).”

“The objectively determined thresholds, based on model output mixing ratios, optimize the performance of the hydrometeor phase classification algorithm and are expected to generate the best (by minimizing false detection) hydrometeor phase classifications. Results using these objective flexible thresholds are compared in Sec. 6.4 to results using the fixed empirical thresholds of Shupe (2007).”

“The performance of the objectively determined flexible phase-classification thresholds (illustrated using colored dashed lines and shading in Fig. 7) is examined against those empirically

derived by Shupe (2007) with one exception (illustrated using grey lines in Fig. 7). The modification to Shupe (2007) is that radar reflectivity larger than 5 dBZ are not associated with the snow category since introducing this assumption was found to increase hydrometeor-phase misclassification (not shown). From Fig. 7 it is apparent that both sets of thresholds are very similar. We estimate that hydrometeor phase frequency of occurrence produced by both threshold sets are within 6.1 % of each other and that the fixed empirical thresholds modified from Shupe (2007) only produce phase misclassification in an additional 0.7 % of hydrometeor-containing grid cells (compare Table 1b to Table 1c). These results suggest that the use of lidar-radar threshold-based techniques for hydrometeor-phase classification depends little on the choice of thresholds.”

**R3. Constructing an ensemble of forward calculations based on different empirical relationships is a good idea, but it is a stretch to portray it as quantifying uncertainty. The authors have no way to know to what extent the results from these calculations actually map to the PDF of possible outcomes. It is useful but is not statistically defensible to call it UQ. The authors should much more carefully word this claim.**

A3. The authors agree with the reviewer that the 576 forward-simulations performed do not cover the entire range of possible scattering assumptions. The following manuscript changes reflect this reality:

“Additionally empirical relationships are computationally less expensive to implement than direct radiative scattering calculations, thus enabling the estimation of an ensemble of backscattering calculations using a range of assumptions in an effort to quantify part of the backscattering uncertainty (see Sec. 7).”

“(GO)<sup>2</sup>-SIM performs an uncertainty assessment by performing an ensemble of 576 forward simulations based on 18 different empirical relationships (relationships are listed in Table 2). While the relationships used do not cover the entire range of possible backscattering assumptions, they represent an attempt at uncertainty quantification and illustrate a framework for doing so. [...] Nevertheless, we suggest using the full range of frequency of occurrences presented in Tables 1b,c for future model evaluation using observations and acknowledge that additional uncertainty is most likely present.”

**R4. The calculations are based on 30-minute instantaneous model hydrometeor fields. The article is focused on the actual forward calculations of the microphysical fields, but comparison of forward-model calculations and observations necessarily includes assumptions of spatial and temporal scale. Would the authors please discuss with a bit more detail on how the forward calculations (30-minute instantaneous calculations of lidar and radar fields) would be compared to observations? If nothing else, this would provide some guidance for readers using their forward simulator.**

A4. We now elaborate more on this topic and provide an updated flow chart:

“A follow-up study will describe an approach by which vertical and temporal resampling of observations can help reduce the scale gap. Furthermore, it will be showed that, using simplified

model evaluation targets based on three atmospheric regions separated by constant pressure levels, ground-based observations can be used for GCM hydrometeor-phase evaluation.”

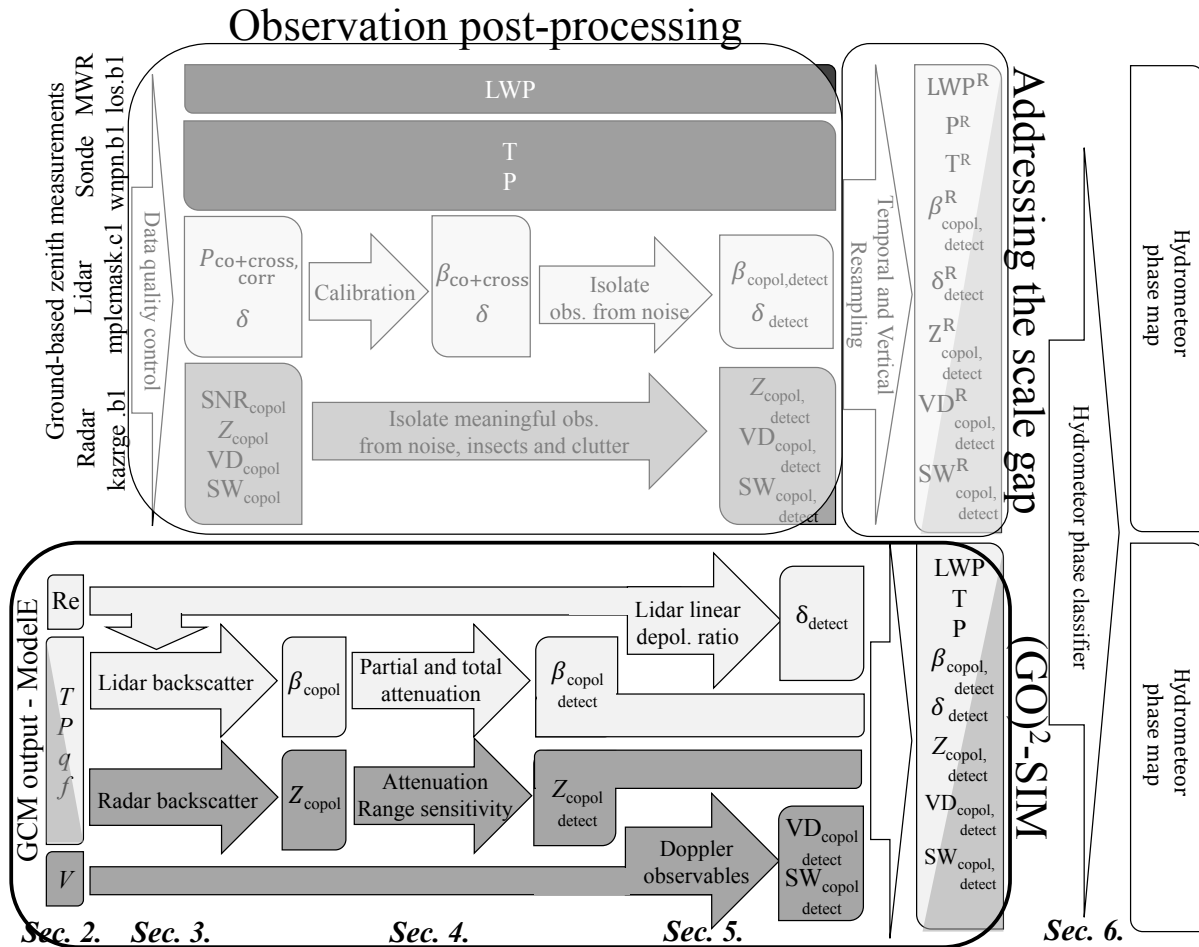


**Figure 1.** (GO)<sup>2</sup>-SIM framework. (GO)<sup>2</sup>-SIM emulates two types of remote sensors: Ka-band Doppler radars (dark gray shading) and 532 nm polarimetric lidars (light gray shading). It then tunes and applies a common phase-classification algorithm (white boxes) to both observed (upper section) and forward-simulated (bottom section) fields. Follow-on work will describe how observation can be post-processed and resampled to reduce the scale gap before model evaluation can be performed.

The authors would like to thank the reviewer for their insightful comments. A point by point response to the reviewer’s comments, along with changes made to the manuscript as a result, are included below.

**R1. Although it is frequently stressed in the manuscript that the radar is very sensible to particle size none of the empirical equations takes the particle size into account.**

A1. The following manuscript changes have been made to address the reviewer’s comment:

“(GO)<sup>2</sup>-SIM relies on water content-based empirical relationships to estimate cloud liquid water (cl), cloud ice (ci), precipitating liquid water (pl) and precipitating ice (pi) radar reflectivity. Different relationships are used for each species to account for the fact that hydrometeor mass and size both affect radar reflectivity.”

“Figure 3b illustrates the fact that for all these empirical relationships increasing water content leads to increasing radar reflectivity. As already mentioned, radar reflectivity is approximately related to the sixth power of the particle size, which explains why, for the same water content, precipitating hydrometeors are associated with greater reflectivity than cloud hydrometeors.”

**R2. The motivation for the ice lidar ratio of 25.7 sr (Eq. 7) is not motivated. Additionally the lidar ratio is often dependent on the particle size which is not addressed in the manuscript.**

A2. The following manuscript changes have been made to address the reviewer’s comment:

“Lidar co-polar backscattered power ( $\beta_{\text{copol,species}} [\text{m}^{-1}\text{sr}^{-1}]$ ) generated by each hydrometeor species is related to lidar extinction ( $\sigma_{\text{copol,species}} [\text{m}^{-1}]$ ) through the lidar ratio ( $S_{\text{species}} [\text{sr}]$ ):

$$\beta_{\text{copol,cl}} = (1/S_{\text{cl}}) \sigma_{\text{copol,cl}}. \quad (6)$$

$$\beta_{\text{copol,ci}} = (1/S_{\text{ci}}) \sigma_{\text{copol,ci}}. \quad (7)$$

While constant values are used for the lidar ratios of liquid and ice clouds in this version of the forward-simulator, we acknowledge that in reality they depend on particle size. O'Connor et al. (2004) suggest that a liquid cloud lidar ratio ( $S_{\text{cl}}$ ) of 18.6 sr is valid for cloud liquid droplets smaller than 25  $\mu\text{m}$ , which encompasses the median diameter expected in the stratiform clouds simulated here. Kuehn et al. (2016) observed layer-averaged lidar ratios in ice clouds ( $S_{\text{ci}}$ ) ranging from 15.1 to 36.3 sr. Sensitivity tests indicate that adjusting the ice cloud lidar ratio to either of these extreme values in the forward-simulator increases the number of detectable hydrometeors by no more than 0.6 %, changes the hydrometeor phase frequency of occurrence statistics by less than 0.4% and causes less than a 0.1% change in phase-classification errors (not shown). Given these results, the ice cloud lidar ratio is set to the constant value of 25.7 sr, which corresponds to the mean value observed by Kuehn et al. (2016)”

**R3. No multiple scattering is simulated even for water clouds or thick ice clouds.**

A3. The following manuscript changes have been made to address the reviewer’s comment:

“Lidar attenuation is exponential and two-way as it affects the lidar power on its way out and back:

$$\beta_{\text{copol,total,att}} = \beta_{\text{copol,total}} e^{-2\eta\tau}. \quad (22)$$

Note that in some instances multiple scattering occurs before the lidar signal returns to the sensor, thus amplifying the returned signal. In theory, the multiple scattering coefficient ( $\eta$ ) varies from 0 to 1. Sensors with large fields of view, such as satellite-based lidars, are more likely to be impacted by multiple scattering than others (Winker, 2003). In the current study, for which a ground-based lidar is simulated, a multiple scattering coefficient of unity is used. A sensitivity test in which this coefficient was varied from 0.7, such as that implemented in the CALIPSO satellite lidar simulator of Chepfer et al. (2008), to 0.3, representing an extreme case, indicated that multiple scattering had a negligible impact (less than 1%) on the number of hydrometeors detected, the hydrometeor phase frequency of occurrence statistics, and in phase classification error (not shown).”

“According to an analysis of CALIPSO observations by Cesana and Chepfer (2013), cloud ice particle cross-polar backscattering ( $\beta_{\text{crosspol,ci,detect}}$  [ $\text{m}^{-1}\text{sr}^{-1}$ ]) and cloud liquid droplet cross-polar backscattering ( $\beta_{\text{crosspol,cl,detect}}$  [ $\text{m}^{-1}\text{sr}^{-1}$ ]) can be approximated using the following relationships:

$$\beta_{\text{crosspol,ci,detect}} = 0.29 (\beta_{\text{copol,ci,detect}} + \beta_{\text{crosspol,ci,detect}}), \quad (26b)$$

$$\beta_{\text{crosspol,cl,detect}} = 1.39 (\beta_{\text{copol,cl,detect}} + \beta_{\text{crosspol,cl,detect}}) + 1.76 \cdot 10^{-2} (\beta_{\text{copol,cl,detect}} + \beta_{\text{crosspol,cl,detect}}) \approx 0. \quad (26c)$$

For reasons mentioned in Sec. 4.1, multiple scattering is considered negligible in the current study such that cloud-liquid droplet cross-polar backscattering is assumed to be zero under all conditions.”

#### **R4. Please give a reference for radar attenuation (Eq. 24b).**

A4. The manuscript was modified to include a reference to Ellis, S. M., and Vivekanandan, J.: Liquid water content estimates using simultaneous S and Ka band radar measurements, Radio Science, 46, 2011:

“At 8.56 mm (Ka-band) total co-polar attenuated reflectivity ( $Z_{\text{copol,total,att}}$  [dBZ]) is given by:

$$Z_{\text{copol,total,att}} = Z_{\text{copol,total}} - 2 \int_{z=0}^z [\alpha (WC_{\text{pl}} + WC_{\text{cl}})] dh, \quad (24)$$

where attenuation is controlled by the wavelength-dependent attenuation coefficient  $\alpha$  ([dB km<sup>-1</sup> (g m<sup>-3</sup>)<sup>-1</sup>]) which we take to be 0.6 at Ka-band (Ellis and Vivekanandan, 2011), by the water contents of cloud liquid ( $WC_{\text{cl}}$  [g m<sup>-3</sup>]) and precipitating liquid ( $WC_{\text{pl}}$  [g m<sup>-3</sup>]), and by the thickness of the liquid layer.”

**R5. The meaning of the terms in Eq. 29 is not completely clear to me. Please give the derivation of Eq. 29.**

A5. A reference to Everitt, B., and Hand, D.: Mixtures of normal distributions, in: Finite Mixture Distributions, Springer, 25-57, 1981 was added. A derivation of the first five central moments of a two-component univariate normal mixture is presented in their book. The following manuscript changes were made to improve clarity:

“Total mean Doppler velocity detected ( $VD_{\text{copol,detect}}$  [ $\text{m s}^{-1}$ ]) is the reflectivity-weighted sum of the mass-weighted fall velocity of each hydrometeor species ( $V_{\text{species}}$  [ $\text{m s}^{-1}$ ]):

$$VD_{\text{copol,detect}} = \sum_{\text{species=cl,pl,ci,pi}} P_{\text{species}} V_{\text{species}}, \quad (28)$$

where the mass-weighted fall velocity of each hydrometeor species ( $V_{\text{species}}$  [ $\text{m s}^{-1}$ ]) is a model output. Total Doppler spectral width ( $SW_{\text{copol,detect}}$  [ $\text{m s}^{-1}$ ]) is more complex and can be estimated following a statistical method similar to that described by Everitt and Hand (1981). It takes into consideration the properties of each individual hydrometeor species through their respective fall speed ( $V_{\text{species}}$  [ $\text{m s}^{-1}$ ]) and spectral width ( $SW_{\text{species}}$  [ $\text{m s}^{-1}$ ]) in relation to the properties of the hydrometeor population as a whole through the total mean Doppler velocity detected ( $VD_{\text{copol,detect}}$ ) estimated in Eq. 28:

$$SW_{\text{copol,detect}} = \sum_{\text{species=cl,pl,ci,pi}} P_{\text{species}} \left( SW_{\text{species}}^2 + (V_{\text{species}} - VD_{\text{copol,detect}})^2 \right), \quad (29)$$

where the spectral widths of individual species ( $SW_{\text{species}}$ ) are assigned climatological values. These climatological values are  $SW_{\text{cl}} = 0.10 \text{ m s}^{-1}$ ,  $SW_{\text{ci}} = 0.05 \text{ m s}^{-1}$ ,  $SW_{\text{pi}} = 0.15 \text{ m s}^{-1}$  and  $SW_{\text{pl}} = 2.00 \text{ m s}^{-1}$  (Kalesse et al., 2016).”

**R6. A number of empirical equations are used to estimate the uncertainties. Although each formula is valuable for specific situations I am not sure if their ensemble covers the whole range of variability of ModelE output. A forward model using the modelled effective radius might help.**

A6. The authors agree with the reviewer that the 576 forward-simulations performed do not cover the entire range of possible scattering assumptions. The following manuscript changes reflect this reality:

“Additionally empirical relationships are computationally less expensive to implement than direct radiative scattering calculations, thus enabling the estimation of an ensemble of backscattering calculations using a range of assumptions in an effort to quantify part of the backscattering uncertainty (see Sec. 7).”

(GO)<sup>2</sup>-SIM performs an uncertainty assessment by performing an ensemble of 576 forward simulations based on 18 different empirical relationships (relationships are listed in Table 2).

While the relationships used do not cover the entire range of possible backscattering assumptions, they represent an attempt at uncertainty quantification and illustrate a framework for doing so. [...] Nevertheless, we suggest using the full range of frequency of occurrences presented in Tables 1b,c for future model evaluation using observations and acknowledge that additional uncertainty is most likely present.”



1 **(GO)<sup>2</sup>-SIM: A GCM-Oriented Ground-Observation Forward-Simulator**  
2 **Framework for Objective Evaluation of Cloud and Precipitation Phase**  
3

4 Katia Lamer<sup>1</sup>, Ann M. Fridlind<sup>2</sup>, Andrew S. Ackerman<sup>2</sup>, Pavlos Kollias<sup>3,4,5</sup>,  
5 Eugene E. Clothiaux<sup>1</sup> and Maxwell Kelley<sup>2</sup>  
6

7 <sup>1</sup> Department of Meteorology and Atmospheric Science, Pennsylvania State University, University Park, 16802, U.S.A.

8 <sup>2</sup> NASA Goddard Institute for Space Studies, New York, 10025, U.S.A.

9 <sup>3</sup> Environmental & Climate Sciences Department, Brookhaven National Laboratory, Upton, 11973, U.S.A.

10 <sup>4</sup> School of Marine and Atmospheric Sciences, Stony Brook University, Stony Brook, 11794, U.S.A.

11 <sup>5</sup> University of Cologne, Cologne, 50937, Germany  
12

13 *Correspondence to:* Katia Lamer ([kx15431@psu.edu](mailto:kx15431@psu.edu))  
14

15  
16 **Abstract**  
17

18 General circulation model (GCM) evaluation using ground-based observations is complicated by  
19 inconsistencies in hydrometeor and phase definitions. Here we describe (GO)<sup>2</sup>-SIM, a forward-simulator  
20 designed for objective hydrometeor phase evaluation, and assess its performance over the North Slope of  
21 Alaska using a one-year GCM simulation. For uncertainty quantification, 18 empirical relationships are  
22 used to convert model grid-average hydrometeor (liquid and ice, cloud and precipitation) water contents to  
23 zenith polarimetric micropulse lidar and Ka-band Doppler radar measurements producing an ensemble of  
24 576 forward-simulation realizations. Sensor limitations are represented in forward space to objectively  
25 remove from consideration model grid cells with undetectable hydrometeor mixing ratios, some of which  
26 may correspond to numerical noise.  
27

28 Phase classification in forward space is complicated by the inability of sensors to measure ice and liquid  
29 signals distinctly. However, signatures exist in lidar-radar space such that thresholds on observables can be  
30 objectively estimated and related to hydrometeor phase. The proposed phase classification technique leads  
31 to misclassification in fewer than 8% of hydrometeor-containing grid cells. Such misclassifications arise  
32 because, while the radar is capable of detecting mixed-phase conditions, it can mistake water- for ice-  
33 dominated layers. However, applying the same classification algorithm to forward-simulated and observed  
34 fields should generate hydrometeor phase statistics with similar uncertainty. Alternatively, choosing to  
35 disregard how sensors define hydrometeor phase leads to frequency of occurrence discrepancies of up to  
36 40%. So, while hydrometeor phase maps determined in forward space are very different from model  
37 “reality” they capture the information sensors can provide and thereby enable objective model evaluation.  
38  
39  
40  
41  
42  
43  
44  
45  
46  
47  
48

49 **1 Introduction**

50

51

52

53

54

55

56

57

58

59

60

61

62

63

64

65

66

67

68

69

70

71

72

73

74

75

76

77

78

79

80

81

82

83

84

85

86

87

88

89

90

91

92

93

94

95

96

97

98

The effect of supercooled water on the Earth's top-of-atmosphere energy budget is a subject of increasing interest owing to its wide variability across climate models and its potential impact on predicted equilibrium climate sensitivity (Tan et al., 2016; McCoy et al., 2016; Frey et al., 2017). Some general circulation models (GCMs) now prognose number concentrations and mass mixing ratios for both cloud and precipitation hydrometeors of both liquid and ice phase, which enables them to shift towards more realistic microphysical process-based phase prediction (e.g., Gettelman and Morrison, 2015; Gettelman et al., 2015). While more complete and physically sound, these models still contain multiple scheme choices and tuning parameters, creating a need for increasingly thorough evaluation and adjustment (e.g., Tan and Storelvmo, 2016; English et al., 2014).

Active remote sensing observations remain an indirect approach to evaluate models because they measure hydrometeor properties different from those produced by microphysical schemes. For each hydrometeor species within a grid cell models prognose geophysical quantities such as mass and number concentration, whereas active remote sensors measure power backscattered from all hydrometeors species present within their observation volumes. Defining which hydrometeors have an impact is a fundamental question that needs to be addressed by the modeling, as well as observational, communities. In numerical models it is not uncommon to find very small hydrometeor mixing ratio amounts as demonstrated below. They may possibly be unphysical, effectively numerical noise, and the decision of which hydrometeor amounts are physically meaningful is somewhat arbitrary. Considering sensor capabilities is one path to objectively assessing hydrometeor populations within models. On such a path it is possible to evaluate those simulated hydrometeor populations that lead to signals detectable by sensors, leaving unassessed those not detected. Sensor detection capabilities are both platform- and sensor-specific. Space-borne lidars can adequately detect liquid clouds globally but their signals cannot penetrate thick liquid layers, limiting their use to a subset of single-layer systems or upper-level cloud decks (Hogan et al., 2004). Space-borne radar observations, while able to penetrate multi-layer cloud systems, are of coarser vertical resolution and of limited value near the surface owing to ground interference and low sensitivity (e.g., Huang et al., 2012b; Battaglia and Delanoë, 2013; Huang et al., 2012a). A perspective from the surface can therefore be more appropriate for the study of low-level cloud systems (e.g., de Boer et al., 2009; Dong and Mace, 2003; Klein et al., 2009; Intrieri et al., 2002).

Fortunately, both sensor sampling and hydrometeor scattering properties can be emulated through the use of forward-simulators. Forward-simulators convert model output to quantities observed by sensors and enable a fairer comparison between model output and observations; discrepancies can then be more readily attributed to dynamical and microphysical differences rather than methodological bias. For example, the CFMIP (Cloud Feedback Model Intercomparison Project) Observation Simulator Package (COSP) is composed of a number of satellite-oriented forward-simulators (Bodas-Salcedo et al., 2011), including a lidar backscattering forward-simulator that has been used to evaluate the representation of upper-level supercooled water layers in GCMs (e.g., Chepfer et al., 2008; Kay et al., 2016). Also, Zhang et al. (2017) present a first attempt at a ground-based radar reflectivity simulator tailored for GCM evaluation.

Here we propose to exploit the complementarity of ground-based vertically pointing polarimetric lidar and Doppler radar measurements, which have been shown uniquely capable of documenting water phase in shallow and multi-layered cloud conditions near the surface where supercooled water layers frequently form. More specifically, we present a GCM-oriented ground-based observation forward-simulator [(GO)<sup>2</sup>-SIM] framework designed for objective hydrometeor phase evaluation (Fig. 1). GCM output variables (Sec. 2) are converted to observables in three steps: 1) hydrometeor backscattered power estimation (Sec. 3), 2) consideration for sensor capabilities (Sec. 4) and, 3) estimation of specialized observables (Sec. 5). These forward-simulated fields, similar to observed fields, are used as inputs to a multi-sensor water phase

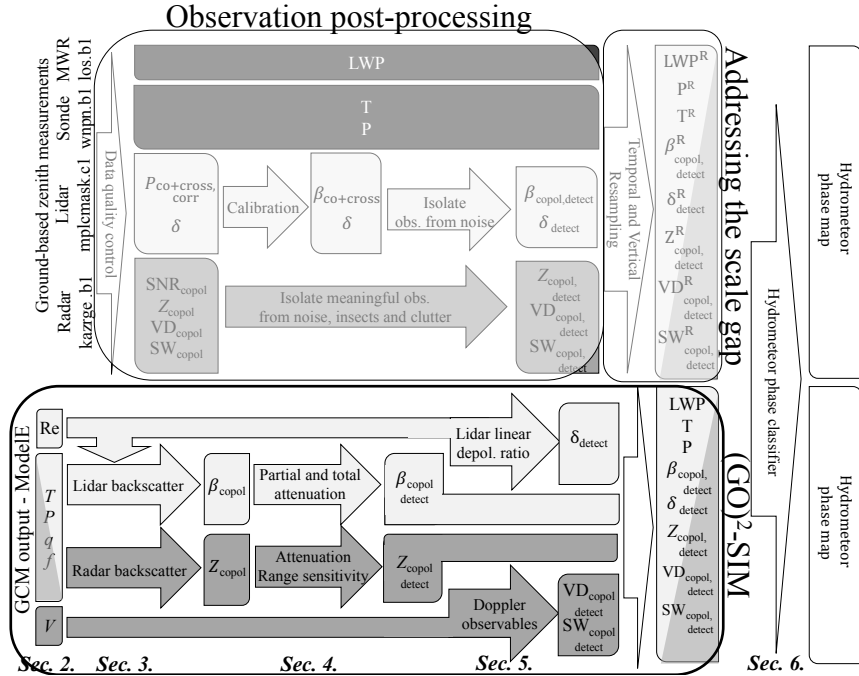


**Figure 1.** (GO)<sup>2</sup>-SIM framework. (GO)<sup>2</sup>-SIM emulates two types of remote sensors: Ka-band Doppler radars (dark gray shading) and 532 nm polarimetric lidars (light gray shading). It then tunes and applies a common phase-classification algorithm (white boxes) to both observed (upper section) and forward-simulated (bottom section) fields. Follow-on work will describe how observation can be post-processed and resampled to reduce the scale gap before model evaluation can be performed.

classifier (Sec. 6). The performance of (GO)<sup>2</sup>-SIM is evaluated over the North Slope of Alaska using output from a one-year simulation of the current development version of the NASA Goddard Institute for Space Studies GCM, hereafter referred to by its generic name, ModelE. Limitations and uncertainty are discussed in Sec. 6.3 and Sec. 7 respectively.

## 2 GCM Outputs Required as Inputs to the Forward-Simulator

To demonstrate how atmospheric model variables are converted to observables we performed a one-year global simulation using the current development version of the ModelE GCM. Outputs from a column over the North Slope of Alaska (column centered at latitude 71.00° and longitude -156.25°) are input to (GO)<sup>2</sup>-SIM. The most relevant changes from a recent version of ModelE (Schmidt et al. 2014) are implementation of the Bretherton and Park (2009) moist turbulence scheme and the Gettelman and Morrison (2015) microphysics scheme for stratiform cloud. The implementation of a two-moment microphysics scheme with prognostic precipitation species makes this ModelE version more suitable for the forward simulations presented here than previous versions. Here ModelE is configured with a 2.0° by 2.5° latitude-longitude grid with 62 vertical layers. The vertical grid varies with height from 10 hPa layer thickness over the bottom 100 hPa of the atmosphere, coarsening to about 50 hPa thickness in the mid-

**Deleted:** treats/

**Deleted:** show how an approach based on cloud vertical structure (CVS)

**Deleted:** can be used as a final step before model evaluation

**Ground-based obs. Radar**

$Z_{copol,detect}$	Significant c
$VD_{copol,detect}$	Com
$SW_{copol,detect}$	
First cloud base height	Insect detection
$\beta_{copol,detect}$	Significant c
$\delta_{detect}$	Com

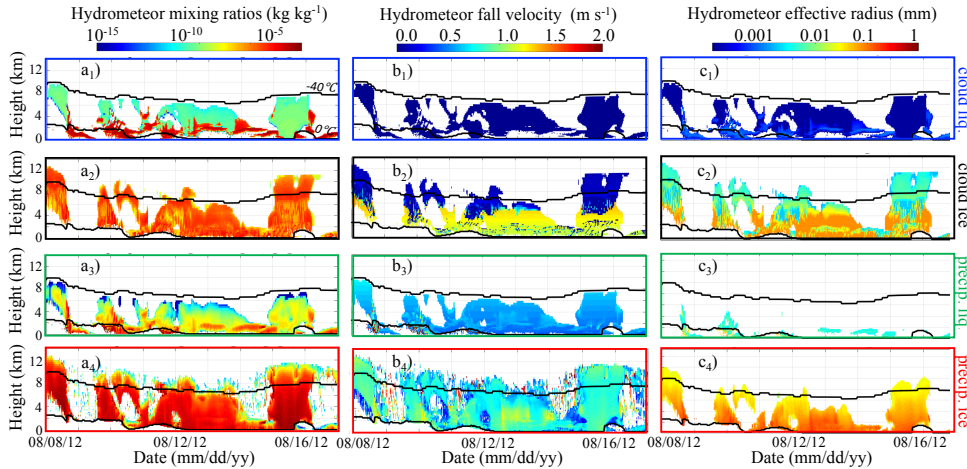
**Lidars**

**Model output Sec. 2.0**

Re			
T	Lidar backscatter	$\beta_{copol}$	Partial and total attenuation
P	Radar backscatter	$Z_{copol}$	Attenuation Range sensitivity
q			
f			
V			

**Sec. 3.0**                      **Sec. 4.0**

**Deleted:** uncertainty quantified in



131

132

133

134

135

136

137

138

139

140

141

142

143

144

145

146

147

148

149

150

151

152

153

154

155

156

157

158

159

160

161

162

**Figure 2.** Sample time series of ModelE outputs: a<sub>1-4</sub>) mixing ratios, b<sub>2-4</sub>) mass weighted fall speed (positive values indicate downward motion) and c<sub>1-4</sub>) effective radii for cloud droplets (1; blue boxes), cloud ice particles (2; black boxes), precipitating liquid drops (3; green boxes) and precipitating ice particles (4; red boxes). Also indicated are the locations of the 0 °C and -40 °C isotherms (horizontal black lines).

troposphere, and refining again to about 10 hPa thickness near the tropopause. For the current study, model top is at 0.1 hPa, though we limit our analysis to pressures greater than 150 hPa. Dynamics (large scale advection) is computed on a 225-s time step and column physics on a 30-min time step. High time-resolution outputs (every column physics time step) are used as input to (GO)<sup>2</sup>-SIM. ModelE relies on two separate schemes to prognose the occurrence of stratiform and convective clouds. The current study focuses on stratiform clouds because their properties are more thoroughly diagnosed in this model version; when performing future model evaluation, the contribution from convective clouds will also be considered.

An example of eight days of this simulation is displayed in Fig. 2. From a purely numerical modelling standpoint, the simplest approach to defining hydrometeors is to consider any nonzero hydrometeor mixing ratio as physically meaningful. Using this approach, we find that 43.5 % of the 981,120 grid cells simulated in the one-year ModelE run contain hydrometeors, with 2.4 % of them being pure liquid, 37.8 % pure ice and 59.8 % mixed in phase (Table 1a). However, these statistics are impacted by a number of simulated small hydrometeor mixing ratio amounts that may or may not result from numerical noise (e.g., Fig. 2a; blue-green colors). The forward-simulator framework will be used to create phase statistics of only those hydrometeors present in amounts that can create signal detectable by sensors hence removing the need for arbitrary filtering.

(GO)<sup>2</sup>-SIM forward-simulator inputs are, at model native resolution, mean grid box temperature and pressure as well as hydrometeor mixing ratios, area fractions (used to estimate in-cloud values), mass weighted fall speeds and effective radii for four hydrometeor species: cloud liquid water, cloud ice, precipitating liquid water and precipitating ice. In its current setup, (GO)<sup>2</sup>-SIM can accommodate any model that produces these output variables

### 163 3 Hydrometeor Backscattered Power Simulator

164

165 Reaching a common objective hydrometeor definition between numerical model output and active sensors  
166 starts by addressing the fact that they are based on different hydrometeor properties (i.e., moments).  
167 Backscattering amounts, observed by sensors, depend on both sensor frequency and on hydrometeors  
168 properties and amounts. Hydrometeor properties that impact backscattering include size, phase,  
169 composition, geometrical shape, orientation and bulk density. Were plausible representations for these  
170 hydrometeor properties available as part of the model formulation, fundamental radiative scattering transfer  
171 calculations would be the most accurate way to transform model hydrometeor properties to observables.  
172 However, in most GCMs such detailed hydrometeor information is highly simplified (e.g., fixed particle  
173 size distribution shapes) or not explicitly represented (e.g., orientation and realistic geometrical shape),  
174 complicating the process of performing direct radiative scattering transfer calculations. Chepfer et al.  
175 (2008) proposed an approach by which lidar backscattered power can be forward-simulated using model  
176 output hydrometeor effective radius. Their approach, based on Mie theory, relies on the assumption that  
177 cloud particles (both liquid and ice) are spherical and requires additional assumptions about hydrometeor  
178 size distributions and scattering efficiencies. Similarly, the COSP (Bodas-Salcedo et al., 2011) and ARM  
179 Cloud Radar Simulator for GCMs (Zhang et al., 2017) packages both use QuickBeam for the estimation of  
180 radar backscattered power (i.e., radar reflectivity; Haynes et al., 2007). QuickBeam computes radar  
181 reflectivity using Mie theory again under the assumption that all hydrometeor species are spherical and by  
182 making additional assumptions about the shape of hydrometeor size distributions as well as mass-size and  
183 diameter-density relationships. While some of these assumptions may be consistent with the assumptions in  
184 model cloud microphysical parameterizations, some are not adequately realistic (e.g., spherical ice) or  
185 complete for accurate backscattering estimation and it is typically very difficult to establish the sensitivity  
186 of results to all such assumptions.

187

188 To avoid having to make ad hoc assumptions about hydrometeor shapes, orientations, and  
189 compositions, which are properties that also remain poorly documented in nature, (GO)<sup>2</sup>-SIM employs  
190 empirical relationships to convert model output to observables. These empirical relationships based on  
191 observations, direct or retrieved with their own sets of underlying assumptions, are expected to capture at  
192 least part of the natural variability in hydrometeor properties. Additionally empirical relationships are  
193 computationally less expensive to implement than direct radiative scattering calculations, thus enabling the  
194 estimation of an ensemble of backscattering calculations using a range of assumptions in an effort to  
195 quantify part of the backscattering uncertainty (see Sec. 7). The empirical relationships proposed require  
196 few model inputs, potentially enhancing consistency in applying (GO)<sup>2</sup>-SIM to models with differing  
197 microphysics scheme assumptions and complexity. Section 6 will show that, while the empirical  
198 relationships employed in (GO)<sup>2</sup>-SIM may not be as exact as direct radiative scattering calculations, they  
199 produce backscattering estimates of sufficient accuracy for hydrometeor phase classification, which is the  
200 main purpose of (GO)<sup>2</sup>-SIM at this time.

201

#### 202 3.1 Lidar Backscattered Power Simulator

203

204 At a lidar wavelength of 532 nm, backscattered power is proportional to total particle cross section per  
205 unit volume. Owing to their high number concentrations, despite their small size, cloud particles  
206 backscatter this type of radiation the most.

207

208 We adopt the Hu et al. (2007b) representation of liquid cloud extinction derived from CALIPSO and  
209 CERES-MODIS observations and retrievals of liquid water content and effective radius (Table 2, Eq. 1).  
210 For cloud ice water content, a number of empirical relationships with lidar extinction have been proposed  
211 for various geophysical locations and ice cloud types using a variety of assumptions. Four of these  
212 empirical relationships are implemented in (GO)<sup>2</sup>-SIM (Table 2, Eqns. 2-5 and references therein) and used

213 **Table 1.** a) Hydrometeor phase frequency of occurrence obtained a) from ModelE mixing ratios outside of  
 214 the forward-simulator framework, b) and c) from the forward simulation ensemble created using different  
 215 backscattered power assumptions. The median and interquartile range (IQR) capture the statistical behavior  
 216 of the ensemble. Results using thresholds b) objectively determined for each forward ensemble member, c)  
 217 modified from those in Shupe (2007). Percentage values are relative either to the total number of simulated  
 218 hydrometeor-containing grid cells (426,603) or those grid cells with detectable hydrometeor amounts  
 219 (333,927). Note that the total number of simulated grid cells analyzed is 981,120.  
 220

a) Determined using ModelE Output Hydrometeor Mixing Ratios								
	Grid cells containing only liquid phase		Grid cells containing mixed phase		Grid cells containing only ice phase		Simulated hydrometeor-containing grid cells	
Frequency of Occurrence (%)	2.4		59.8		37.8		43.5	
b) Determined Using Flexible Objective Thresholds from Model Output Mixing-Ratios								
	Grid cells classified as liquid phase		Grid cells classified as mixed phase		Grid cells classified as ice phase		Grid cells containing detectable hydrometeors	
	Median	$\frac{1}{2}$ IQR	Median	$\frac{1}{2}$ IQR	Median	$\frac{1}{2}$ IQR	Median	$\frac{1}{2}$ IQR
Frequency of Occurrence (%)	11.3	$\pm 0.6$	19.2	$\pm 1.8$	68.8	$\pm 3.1$	78.3	$\pm 1.8$
False Positive (%)	0.5	$\pm 0.0$	1.1	$\pm 0.3$	0.0	$\pm 0.0$	1.7	$\pm 0.3$
False Negative (%)	0.2	$\pm 0.0$	See questionable row		1.5	$\pm 0.2$	1.7	$\pm 0.3$
Questionable (%)	1.4	$\pm 0.0$			3.8	$\pm 0.9$	5.2	$\pm 0.9$
Total Error (%)							6.9	$\pm 1.1$
c) Determined Using Fixed Empirical Thresholds Modified from Shupe (2007)								
	Grid cells classified as liquid phase		Grid cells classified as mixed phase		Grid cells classified as ice phase		Grid cells containing detectable hydrometeors	
	Median	$\frac{1}{2}$ IQR	Median	$\frac{1}{2}$ IQR	Median	$\frac{1}{2}$ IQR	Median	$\frac{1}{2}$ IQR
Frequency of Occurrence (%)	12.5	$\pm 0.4$	13.1	$\pm 2.4$	71.5	$\pm 3.7$	78.2	$\pm 1.8$
False Positive (%)	0.5	$\pm 0.0$	0.3	$\pm 0.0$	0.1	$\pm 0.0$	0.9	$\pm 0.0$
False Negative (%)	0.1	$\pm 0.0$	See questionable row		0.7	$\pm 0.0$	0.9	$\pm 0.0$
Questionable (%)	1.4	$\pm 0.0$			5.3	$\pm 1.1$	6.7	$\pm 1.1$
Total Error (%)							7.6	$\pm 1.1$

221  
 222 to generate an ensemble of forward-simulations. Using these empirical relationships, a given water content  
 223 can be mapped to a range of lidar extinction values (Fig. 3a). This spread depends both on the choice of  
 224 empirical relationships and on the variability of the atmospheric conditions that affect them (i.e.,  
 225 atmospheric temperature and hydrometeor effective radius variability). Fig. 3a also illustrates the  
 226 fundamental idea that lidar extinction increases with increasing water content and that for a given water  
 227 content cloud droplets generally lead to higher lidar extinction than cloud ice particles.  
 228

229 Lidar co-polar backscattered power ( $\beta_{\text{copol,species}}$  [ $\text{m}^{-1}\text{sr}^{-1}$ ]) generated by each hydrometeor species is  
 230 related to lidar extinction ( $\sigma_{\text{copol,species}}$  [ $\text{m}^{-1}$ ]) through the lidar ratio ( $S_{\text{species}}$  [sr]):

231  
 232 
$$\beta_{\text{copol,cl}} = (1/S_{\text{cl}}) \sigma_{\text{copol,cl}} \quad (6)$$

233 
$$\beta_{\text{copol,ci}} = (1/S_{\text{ci}}) \sigma_{\text{copol,ci}} \quad (7)$$

Deleted: These relationships will be used to create an ensemble of forward simulations that will be used for uncertainty quantification (see Sec. 7).

Deleted: 18.6 sr

Deleted: (O'Connor et al., 2004)

Deleted: 25.7

Deleted: sr

Deleted: (Kuehn et al., 2016)

While constant values are used for the lidar ratios of liquid and ice clouds in this version of the forward-simulator, we acknowledge that in reality they depend on particle size. O'Connor et al. (2004) suggest that a liquid cloud lidar ratio ( $S_{cl}$ ) of 18.6 sr is valid for cloud liquid droplets smaller than 25  $\mu\text{m}$ , which encompasses the median diameter expected in the stratiform clouds simulated here. Kuehn et al. (2016) observed layer-averaged lidar ratios in ice clouds ( $S_{ci}$ ) ranging from 15.1 to 36.3 sr. Sensitivity tests indicate that adjusting the ice cloud lidar ratio to either of these extreme values in the forward-simulator increases the number of detectable hydrometeors by no more than 0.6 %, changes the hydrometeor phase frequency of occurrence statistics by less than 0.4% and causes less than a 0.1% change in phase-classification errors (not shown). Given these results, the ice cloud lidar ratio is set to the constant value of 25.7 sr, which corresponds to the mean value observed by Kuehn et al. (2016).

It is important to consider that lidars do not measure cloud droplet backscattering independently of cloud ice particle backscattering. Rather they measure total co-polar backscattered power ( $\beta_{\text{copol,total}}$ ) which the sum of the contribution from both cloud phases.

### 3.2 Radar Backscattered Power Simulator

At the cloud-radar wavelength of 8.56 mm (Ka-band), backscattered power is approximately related to the sixth power of the particle diameter, and inversely proportional to the fourth power of the wavelength. Hereafter radar backscattered power will be referred to as “radar reflectivity” as commonly done in literature.

(GO)<sup>2</sup>-SIM relies on water content-based empirical relationships to estimate cloud liquid water (cl), cloud ice (ci), precipitating liquid water (pl) and precipitating ice (pi) radar reflectivity. Different relationships are used for each species to account for the fact that hydrometeor mass and size both affect radar reflectivity. A number of empirical relationships link hydrometeor water content to co-polar radar reflectivity. Thirteen of these empirical relationships are implemented in (GO)<sup>2</sup>-SIM (Table 2, Eqns. 8-20 and references therein) and used to generate an ensemble of forward-simulations. Figure 3b illustrates the fact that for all these empirical relationships increasing water content leads to increasing radar reflectivity. As already mentioned, radar reflectivity is approximately related to the sixth power of the particle size, which explains why, for the same water content, precipitating hydrometeors are associated with greater reflectivity than cloud hydrometeors.

In reality, radars cannot isolate energy backscattered by individual hydrometeor species. Rather they measure total co-polar reflectivity ( $Z_{\text{copol,total}}$  [ $\text{mm}^6 \text{m}^{-3}$ ]) which is the sum of the contributions from all of the hydrometeor species.

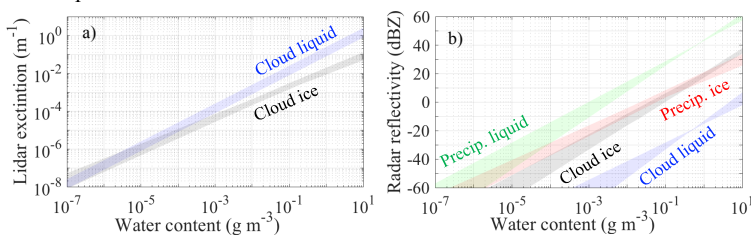


**Figure 3.** Relationship between water content in the form of cloud liquid (blue), precipitating liquid (green), cloud ice (black) and precipitating ice (red) and a) Lidar extinction, and b) Radar co-polar reflectivity. Spread emerges from using multiple differing empirical relationships (listed in Table 2) and from variability in the one-year ModelE output (including the effects of varying temperature and effective radii).

Deleted: Of course,

Deleted: In contrast,

Deleted: It is expected that these empirical relationships capture at least part of the impacts of hydrometeor non-sphericity and inhomogeneity.

Deleted: . These relationships are used to create an ensemble of forward simulations for uncertainty quantification (see Sec. 7).

Deleted: diameter

Deleted: water

Deleted: water

Deleted: and precipitation

Deleted: and ice

Deleted: precipitation

Deleted: snow

Deleted: as a function of water content in the form of water cloud (blue) and ice cloud (black).

Deleted: as a function of water content in the form of water cloud (blue) and precipitation (green) and ice cloud (black) and precipitation (red).

305 **Table 2.** Empirical relationships used to convert hydrometeor water content (WC [g m<sup>-2</sup>]) to lidar  
 306 extinction ( $\sigma$  [m<sup>-1</sup>]) and radar reflectivity ( $Z$  [mm<sup>6</sup> m<sup>-3</sup>]).  
 307

Type	Eq. #	Relationships for lidar extinction	References
Cloud liq. (cl)	1	$\sigma_{\text{copol,cl}} = \frac{\text{WC}_{\text{cl}}(3/2)}{\text{Re } \rho_{\text{liq}}}$ with $\rho_{\text{liq}} = 1$	Hu et al. (2007b)
	2	$\sigma_{\text{copol,cl}} = \left(\frac{\text{WC}_{\text{cl}}}{119}\right)^{1/1.22}$	Heymsfield et al. (2005)
Cloud ice (ci)	3	$\sigma_{\text{copol,ci}} = \left(\frac{\text{WC}_{\text{ci}}}{a_3}\right)^{1/b_3}$ with $a_3 = 89 + 0.6204T$ and $b_3 = 1.02 - 0.0281T$	Heymsfield et al. (2005)
	4	$\sigma_{\text{copol,ci}} = \left(\frac{\text{WC}_{\text{ci}}}{527}\right)^{1/1.32}$	Heymsfield et al. (2014)
	5	$\sigma_{\text{copol,ci}} = \left(\frac{\text{WC}_{\text{ci}}}{a_2}\right)^{1/b_2}$ with $a_2 = 0.00532 * (T + 90)^{2.55}$ and $b_2 = 1.31e^{(0.0047T)}$	Heymsfield et al. (2014)
Type	Eq. #	Relationships for radar reflectivity	References
Cloud liq. (cl)	8	$Z_{\text{copol,cl}} = 0.048 \text{WC}_{\text{cl}}^{2.00}$	Atlas (1954)
	9	$Z_{\text{copol,cl}} = 0.03 \text{WC}_{\text{cl}}^{1.31}$	Sauvageot and Omar (1987)
	10	$Z_{\text{copol,cl}} = 0.031 \text{WC}_{\text{cl}}^{1.56}$	Fox and Illingworth (1997)
Cloud ice (ci)	11a	$Z_{\text{copol,ci}} = 10^{\left(\frac{\log_{10}(\text{WC}_{\text{ci}})+1.70+0.0233T}{0.072}\right)/10}$	R. J. Hogan et al. (2006)
	12	$Z_{\text{copol,ci}} = \left(\frac{\text{WC}_{\text{ci}}}{0.064}\right)^{\frac{1}{0.58}}$	Atlas et al. (1995)
	13	$Z_{\text{copol,ci}} = \left(\frac{\text{WC}_{\text{ci}}}{0.097}\right)^{\frac{1}{0.59}}$	Liu and Illingworth (2000)
	14	$Z_{\text{copol,ci}} = \left(\frac{\text{WC}_{\text{ci}}}{0.037}\right)^{\frac{1}{0.696}}$	Sassen (1987)
Precip. liq. (pl)	15	$Z_{\text{copol,pl}}[\text{mm}^6 \text{m}^{-3}] = \left(\frac{\text{WC}_{\text{pl}}}{0.0034}\right)^{\frac{7}{4}}$	Hagen and Yuter (2003)
	16	$Z_{\text{copol,pl}}[\text{mm}^6 \text{m}^{-3}] = \left(\frac{\text{WC}_{\text{pl}}}{0.0039}\right)^{\frac{1}{0.55}}$	Battan (1973)
	17	$Z_{\text{copol,pl}} = \left(\frac{\text{WC}_{\text{pl}}}{0.00098}\right)^{\frac{1}{0.7}}$	Sekhon and Srivastava (1971)
Precip. ice (pi)	11b	$Z_{\text{copol,pi}} = 10^{\left(\frac{\log_{10}(\text{WC}_{\text{pi}})+1.70+0.0233T}{0.072}\right)/10}$	R. J. Hogan et al. (2006)
	18	$Z_{\text{copol,pi}} = \left(\frac{\text{WC}_{\text{pi}}}{0.0218}\right)^{\frac{1}{0.79}}$	Liao and Sassen (1994)
	19	$Z_{\text{copol,pi}} = \left(\frac{\text{WC}_{\text{pi}}}{0.04915}\right)^{\frac{1}{0.90}}$	Sato et al. (1981)
	20	$Z_{\text{copol,pi}} = \left(\frac{\text{WC}_{\text{pi}}}{0.05751}\right)^{\frac{1}{0.736}}$	Kikuchi et al. (1982)



## 308 4 Sensor Capability Simulator

309

310 In the previous section, total backscattered power resulting from all modeled hydrometeor species  
311 (without any filtering) is estimated. In order to objectively assess model hydrometeor properties, they must  
312 be converted to quantities that are comparable to observations, necessitating incorporation of sensor  
313 detection limitations, including attenuation and finite sensitivity. Fortunately, lidar and radar sensors are  
314 often relatively well-characterized so that sensor detection capabilities can be quantified and replicated in  
315 forward-simulators for an objective model-to-observation comparison.

316

### 317 4.1 Lidar Detection Capability

318

319 Following the work of [Chepfer et al. \(2008\)](#), the (GO)<sup>2</sup>-SIM lidar forward-simulator takes into  
320 consideration that lidar power is attenuated by clouds. Attenuation is related to cloud optical depth ( $\tau$ ),  
321 which is a function of total cloud extinction ( $\sigma_{\text{copol,total}}$  [ $\text{m}^{-1}$ ]) that includes the effect of cloud liquid  
322 water and cloud ice via:

323

$$324 \tau = \int_{z_0}^z \sigma_{\text{copol,total}} dh, \quad (21)$$

325

326 Lidar attenuation is exponential and two-way as it affects the lidar power on its way out and back:

327

$$328 \beta_{\text{copol,total,att}} = \beta_{\text{copol,total}} e^{-2\eta\tau}. \quad (22)$$

329

330 Note that in some instances multiple scattering occurs before the lidar signal returns to the sensor, thus  
331 amplifying the returned signal. In theory, the multiple scattering coefficient ( $\eta$ ) varies from 0 to 1. Sensors  
332 with large fields of view, such as satellite-based lidars, are more likely to be impacted by multiple  
333 scattering than others (Winker, 2003). In the current study, for which a ground-based lidar is simulated, a  
334 multiple scattering coefficient of unity is used. A sensitivity test in which this coefficient was varied from  
335 0.7, such as that implemented in the CALIPSO satellite lidar simulator of Chepfer et al. (2008), to 0.3,  
336 representing an extreme case, indicated that multiple scattering had a negligible impact (less than 1%) on  
337 the number of hydrometeors detected, the hydrometeor phase frequency of occurrence statistics, and in  
338 phase classification error (not shown).

339

340 In the current simulator we assume that only cloud segments with optical depth smaller than three can be  
341 penetrated, other clouds being opaque (Cesana and Chepfer, 2013) such that total co-polar backscattered  
342 power detected ( $\beta_{\text{copol,total,detect}}$ ) is:

343

$$344 \beta_{\text{copol,total,detect}} = \beta_{\text{copol,total,att}} \quad \text{where } \tau \leq 3; \\ 345 \beta_{\text{copol,total,detect}} = \text{undetected} \quad \text{where } \tau > 3. \quad (23)$$

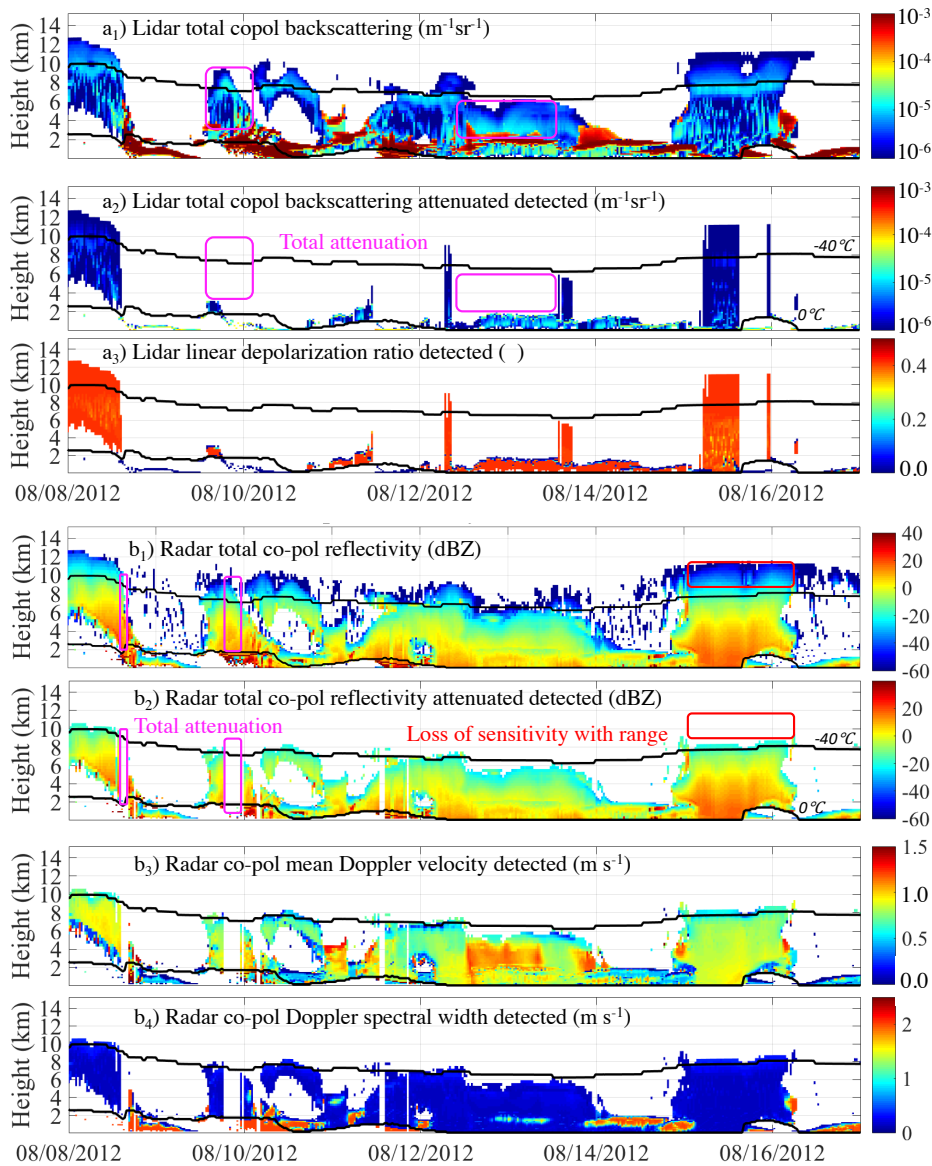
346

347 For the sample ModelE output shown in Fig. 2, Fig. 4a illustrates results from the lidar forward-simulator  
348 for one forward-ensemble member (i.e., using a single set of lidar backscattered power empirical  
349 relationships specifically eqns. (1) and (4)). Figure 4a<sub>1</sub> shows lidar total co-polar backscattered power  
350 without consideration of sensor limitations, such as attenuation, which are included in Fig. 4a<sub>2</sub>. Lidar  
351 attenuation prevents the tops of deep systems containing supercooled water layers from being observed  
352 (e.g., magenta boxes on 08/10 and 08/13). For the one-year sample the forward-simulated lidar system  
353 detects only 35.5% of simulated hydrometeor-containing grid cells. In Sec. 6 we will determine which  
354 hydrometeors (liquid water or ice) are responsible for the detected signals.

355

356

Deleted: Cesana and Chepfer (2013)



358  
 359 **Figure 4.** Example outputs from the (GO)<sup>2</sup>-SIM backscattered power modules (1), sensor capability  
 360 modules (2) and specialized-observables modules (3-4) for a) lidars and b) radars obtained using one set of  
 361 empirical backscattered power relationships. This figure highlights sensor limitations ranging from  
 362 attenuation (magenta boxes) to sensitivity loss with range (red boxes). Also indicated are the locations of  
 363 the 0 °C and -40 °C isotherms (black lines). Note that positive velocities indicate downward motion.

## 4.2 Radar Detection Capability

Millimeter-wavelength radars are also affected by signal attenuation. Radar signal attenuation depends both on the transmitted wavelength and on the mass and phase of the hydrometeors. Liquid phase hydrometeors attenuate radar signals at all millimeter radar wavelengths, even leading to total signal loss in heavy rain conditions. In contrast, water vapor attenuation is less important at relatively longer wavelengths (e.g., 8.56 mm; the wavelength simulated here) but can be important near wavelengths of 3.19 mm (the CloudSat operating wavelength; (Bodas-Salcedo et al., 2011)).

At 8.56 mm (Ka-band) total co-polar attenuated reflectivity ( $Z_{\text{copol,total,att}}$  [dBZ]) is given by:

$$Z_{\text{copol,total,att}} = Z_{\text{copol,total}} - 2 \int_{z=0}^z [a (WC_{\text{pl}} + WC_{\text{cl}})] dh, \quad (24)$$

where attenuation is controlled by the wavelength-dependent attenuation coefficient  $a$  ( $[\text{dB km}^{-1} (\text{g m}^{-3})^{-1}]$ ) which we take to be 0.6 at Ka-band (Ellis and Vivekanandan, 2011), by the water contents of cloud liquid ( $WC_{\text{cl}}$  [ $\text{g m}^{-3}$ ]) and precipitating liquid ( $WC_{\text{pl}}$  [ $\text{g m}^{-3}$ ]), and by the thickness of the liquid layer.

In addition to attenuation, radars suffer from having a finite sensitivity that decreases with distance. Given this, the total co-polar reflectivity detectable ( $Z_{\text{copol,total,detect}}$  [dBZ]) is

$$\begin{aligned} Z_{\text{copol,total,detect}} &= Z_{\text{copol,total,att}} \text{ where } Z_{\text{copol,total,att}} \geq Z_{\text{min}}, \\ Z_{\text{copol,total,detect}} &= \text{Undetected} \text{ where } Z_{\text{copol,total,att}} < Z_{\text{min}}, \end{aligned} \quad (25a)$$

where the radar minimum detectable signal ( $Z_{\text{min}}$  [dBZ]) is a function of height ( $h$  [km]) and can be expressed as

$$Z_{\text{min}} = Z_{\text{sensitivity at 1 km}} + 20 \log_{10} h. \quad (25b)$$

A value of  $Z_{\text{sensitivity at 1 km}} = -41$  dBZ is selected to reflect the sensitivity of the Ka-band ARM Zenith Radar (KAZR) currently installed at the Atmospheric Radiation Measurement (ARM) North Slope of Alaska observatory. This value has been determined by monitoring two years of observations and it reflects the minimum signal observed at a height of 1 km. The minimum detectable signal used in the simulator should reflect the sensitivity of the sensor used to produce the observational benchmark to be compared to the forward-simulator output.

For the sample ModelE output shown in Fig. 2, Figure 4b illustrates results from the radar forward-simulator for one forward-ensemble member (i.e., using a single set of radar reflectivity empirical relationships specifically eqns. (9), (11a), (15) and (11b)). Figure 4b<sub>1</sub> shows radar total co-polar reflectivity without consideration of sensor limitations, while Fig. 4b<sub>2</sub> includes the effects of attenuation and the range-dependent minimum detectable signal. Sensor limitations make it such that heavy rain producing systems cannot be penetrated (e.g., magenta box on 08/08 and 08/10) and the tops of deep systems cannot be observed (e.g., red box on 08/15). For the one-year sample the forward-simulated radar system could detect only 69.9 % of the simulated hydrometeor-containing grid cells. In Sec. 6 we will determine the phase of the hydrometeors responsible for the detected signals.

## 4.3 Lidar-Radar Complementarity

Figures 4a<sub>2</sub> and 4b<sub>2</sub> highlight the complementarity of lidar and radar sensors. Despite sensor limitations, 532 nm lidar measurements can be used to characterize hydrometeors near the surface and infer

**Deleted:** At 8.56 mm (Ka-band) total co-polar attenuated reflectivity ( $Z_{\text{copol,total,att}}$  [dBZ]) is given by

$$Z_{\text{copol,total,att}} = Z_{\text{copol,total}} - a_{\text{cl+pl}} \quad (24a)$$

where cloud and precipitating liquid water contents ( $WC_{\text{cl}}$  and  $WC_{\text{pl}}$  [ $\text{g m}^{-3}$ ]) and the thickness of the liquid layer ( $dh$  [m]): two-way liquid attenuation ( $a_{\text{cl+pl}}$  [dB]) is estimated using cloud and precipitating liquid water contents ( $WC_{\text{cl}}$  and  $WC_{\text{pl}}$  [ $\text{g m}^{-3}$ ]) and the thickness of the liquid layer ( $dh$  [m]):

**Moved (insertion) [1]**

**Moved up [1]:** cloud and precipitating liquid water contents ( $WC_{\text{cl}}$  and  $WC_{\text{pl}}$  [ $\text{g m}^{-3}$ ]) and the thickness of the liquid layer ( $dh$  [m]):

$$\text{Deleted: } a_{\text{cl+pl}} = 2 \int_{z=0}^z [0.6 (WC_{\text{pl}} + WC_{\text{cl}})] dh. \quad (24b)$$

431 the location of a lowermost liquid layer if one exists. In contrast, 8.56 mm radars have the ability to  
 432 penetrate cloud layers and light precipitation, allowing them to determine cloud boundary locations (e.g.  
 433 Kollias et al., 2016). For the one-year sample ModelE output the combination of both sensors enables  
 434 detection of 73.0 % of the hydrometeor-containing grid cells. Real observations can be used to objectively  
 435 evaluate these detectable hydrometeor populations while nothing can be said about those that are not  
 436 detectable. Note that a number of undetectable grid cells only contain trace amounts of hydrometeors,  
 437 which could be the result of numerical noise. As such the approach of considering sensor detection  
 438 limitations helps objectively remove numerical noise from consideration and allows model and  
 439 observations to converge towards a common hydrometeor definition for a fair comparison.

## 441 5 Forward Simulation of Specialized Observables

442  
 443 In the previous section total co-polar backscattered powers are used to determine which simulated  
 444 hydrometeors are present in sufficient amounts to be detectable by sensors hence removing numerical noise  
 445 from consideration. However, determining the phase of the detectable hydrometeor populations can be  
 446 achieved with much greater accuracy by using additional observables.

447  
 448 Backscattered power alone provides a sense of hydrometeor number concentration (from lidar) and  
 449 hydrometeor size (from radar), but it does not contain information about hydrometeor shape nor does it  
 450 provide any hint on the number of coexisting hydrometeor species, both of which are relevant for phase  
 451 determination. However, such information is available from lidar depolarization ratios and radar Doppler  
 452 spectral widths.

### 454 5.1 Lidar Depolarization Ratio Simulator

455  
 456 So far we have described how hydrometeors of all types and phases affect co-polar radiation. It is  
 457 important to note that radiation also has a cross-polar component which is only affected by nonspherical  
 458 particles. Ice particles, which tend to be nonspherical, are expected to affect this component while we  
 459 assume that cloud droplets, which tend to be spherical, do not. Taking the ratio of cross-polar to co-polar  
 460 backscattering thus provides information about the dominance of ice particles in a hydrometeor population.  
 461 This ratio is referred to as the linear depolarization ratio ( $\delta_{\text{detect}}$ ) and it can be estimated where  
 462 hydrometeors are detected by the lidar.

$$463 \delta_{\text{detect}} = \frac{\beta_{\text{crosspol,ci,detect}} + \beta_{\text{crosspol,cl,detect}}}{\beta_{\text{copol,total,detect}}} \quad (26a)$$

464  
 465 According to an analysis of CALIPSO observations by Cesana and Chepfer (2013), cloud ice particle  
 466 cross-polar backscattering ( $\beta_{\text{crosspol,ci,detect}}$  [ $\text{m}^{-1}\text{sr}^{-1}$ ]) and cloud liquid droplet cross-polar  
 467 backscattering ( $\beta_{\text{crosspol,cl,detect}}$  [ $\text{m}^{-1}\text{sr}^{-1}$ ]) can be approximated using the following relationships:

$$470 \beta_{\text{crosspol,ci,detect}} = 0.29 (\beta_{\text{copol,ci,detect}} + \beta_{\text{crosspol,ci,detect}}) \quad (26b)$$

$$471 \beta_{\text{crosspol,cl,detect}} = 1.39 (\beta_{\text{copol,cl,detect}} + \beta_{\text{crosspol,cl,detect}}) \\ 472 + 1.76 \cdot 10^{-2} (\beta_{\text{copol,cl,detect}} + \beta_{\text{crosspol,cl,detect}}) \approx 0 \quad (26c)$$

473  
 474 For reasons mentioned in Sec. 4.1, multiple scattering is considered negligible in the current study such that  
 475 cloud-liquid droplet cross-polar backscattering is assumed to be zero under all conditions.

Deleted: ca

Deleted: According to Cesana and Chepfer (2013) analysis of CALIPSO observations, cloud ice particle cross-polar backscattering ( $\beta_{\text{crosspol,ci,detect}}$  [ $\text{m}^{-1}\text{sr}^{-1}$ ]) can be approximated using the following relationship:

$$\beta_{\text{crosspol,ci,detect}} = \frac{0.29}{1-0.29} \beta_{\text{copol,ci,detect}}$$

Deleted: (26b)

For the sample ModelE output shown in Fig. 2, Fig. 4a<sub>3</sub> shows an example of forward-simulated lidar linear depolarization ratios estimated using one set of backscattered power empirical relationships.

492 **5.2 Radar Doppler Moment Simulator**

493

494 Specialty Doppler radars have the capability to provide information about the movement of  
 495 hydrometeors in the radar observation volume. This information comes in the form of the radar Doppler  
 496 spectrum, which describes how backscattered power is distributed as a function of hydrometeor velocity  
 497 (Kollias et al., 2011). The zeroth moment of the Doppler spectral distribution (the spectral integral) is radar  
 498 reflectivity, the first moment (the spectral mean) is mean Doppler velocity (VD) and the second moment  
 499 (the spectral spread) is Doppler spectral width (SW). Rich information is provided by the velocity spread  
 500 (i.e., SW) of the hydrometeor population including information regarding the number of coexisting species,  
 501 turbulence intensity and spread of the hydrometeor particle size distributions. Typically, the effects of  
 502 turbulence and hydrometeor size variations on the velocity spread for a single species are much smaller  
 503 than the effect of mixed-phase conditions. As such, Doppler spectral width is a useful parameter for  
 504 hydrometeor phase identification.

505

506 Forward-simulations of Doppler quantities have been performed for cloud models using bin microphysics  
 507 (e.g., Tatarevic and Kollias, 2015) but not, to our knowledge, for GCMs using 2-moment microphysics  
 508 schemes. Co-polar mean Doppler velocity and co-polar Doppler spectral width are subject to the same  
 509 detection limitations as radar reflectivity. In fact, just like radar reflectivity, these observables are strongly  
 510 influenced by large hydrometeors; that is, they are reflectivity-weighted velocity averages.

511

512 Our approach begins by quantifying the contribution of each species present ( $P_{\text{species}}$ ), which is determined  
 513 by the species detected co-polar reflectivity ( $Z_{\text{copol,species,detect}}$  [ $\text{mm}^6 \text{m}^{-3}$ ]) relative to the total detected  
 514 co-polar reflectivity ( $Z_{\text{copol,total,detect}}$  [ $\text{mm}^6 \text{m}^{-3}$ ]):

515

516 
$$P_{\text{species}} = \frac{Z_{\text{copol,species,detect}}}{Z_{\text{copol,total,detect}}}, \quad (27a)$$

517

518 together with

519

520 
$$Z_{\text{copol,species,detect}} = Z_{\text{copol,species}} - 2 \int_{Z=0}^Z [a (WC_{\text{pl}} + WC_{\text{cl}})] dh \quad \text{where } Z_{\text{copol,total,att}} \geq Z_{\text{min}}. \quad (27b)$$

521

522 In Eqns. 27a-b the subscript “species” represents cl, ci, pl, or pi. The attenuation coefficient ( $a$ ), minimum  
 523 detectable signal ( $Z_{\text{min}}$ ) and water contents (WC) are as in Eq. 24. Total mean Doppler velocity detected  
 524 ( $VD_{\text{copol,detect}}$  [ $\text{m s}^{-1}$ ]) is the reflectivity-weighted sum of the mass-weighted fall velocity of each  
 525 hydrometeor species ( $V_{\text{species}}$  [ $\text{m s}^{-1}$ ]):

526

527 
$$VD_{\text{copol,detect}} = \sum_{\text{species=cl,pl,ci,pi}} P_{\text{species}} V_{\text{species}}, \quad (28)$$

528

529 where the mass-weighted fall velocity of each hydrometeor species ( $V_{\text{species}}$  [ $\text{m s}^{-1}$ ]) is a model output.  
 530 Total Doppler spectral width ( $SW_{\text{copol,detect}}$  [ $\text{m s}^{-1}$ ]) is more complex and can be estimated following a  
 531 statistical method similar to that described by Everitt and Hand (1981). It takes into consideration the  
 532 properties of each individual hydrometeor species through their respective fall speed ( $V_{\text{species}}$  [ $\text{m s}^{-1}$ ]) and  
 533 spectral width ( $SW_{\text{species}}$  [ $\text{m s}^{-1}$ ]) in relation to the properties of the hydrometeor population as a whole  
 534 through the total mean Doppler velocity detected ( $VD_{\text{copol,detect}}$ ) estimated in Eq. 28:

535

536 
$$SW_{\text{copol,detect}} = \sum_{\text{species=cl,pl,ci,pi}} P_{\text{species}} \left( SW_{\text{species}}^2 + (V_{\text{species}} - VD_{\text{copol,detect}})^2 \right), \quad (29)$$

Deleted:  $Z_{\text{copol,species,detect}} = Z_{\text{copol,species}} - a_{\text{cl+pl}}$ , where  $Z_{\text{copol,total,att}} \geq Z_{\text{min}}$ . (27b)

Deleted:

Deleted: Attenuation

Deleted:  $\text{cl+pl}$

Deleted: and

where the spectral widths of individual species ( $SW_{\text{species}}$ ) are assigned climatological values. These climatological values are  $SW_{\text{cl}} = 0.10 \text{ m s}^{-1}$ ,  $SW_{\text{ci}} = 0.05 \text{ m s}^{-1}$ ,  $SW_{\text{pi}} = 0.15 \text{ m s}^{-1}$  and  $SW_{\text{pl}} = 2.00 \text{ m s}^{-1}$  (Kalesse et al., 2016).

For the sample ModelE output shown in Fig. 2, Figs. 4b<sub>3</sub> and 4b<sub>4</sub> respectively show examples of forward simulated mean Doppler velocity and Doppler spectral width estimate using one set of empirical radar reflectivity relationship.

## 6 Water Phase Classifier Algorithm

From a purely numerical modeling perspective the simplest approach to defining the phase of a hydrometeor population contained in grid cells is to consider that any nonzero hydrometeor mixing ratio species contributes to the phase of the population. Using this approach, in the one-year sample, we find that the detectable hydrometeor-containing grid cells are 2.4 % pure liquid, 19.4 % pure ice and 78.2 % mixed phase (Note how these water phase statistics differ by up to 18.4 % from Sec. 2 where all grid cells, potentially including numerical noise, were considered). But determining hydrometeor phase in observational space is not as straightforward. It is complicated by the fact that sensors do not record ice- and liquid-hydrometeor returns separately but rather record total backscattering from all hydrometeors. Retrieval algorithms are typically applied to the observed total backscattering to determine the phase of hydrometeor populations. However, phase classification algorithms have limitations that require each hydrometeor species to be present not only in nonzero amounts but in amounts sufficient to produce a phase signal. Thus, hydrometeor phase statistics obtained from a numerical model in the absence of a forward simulator are not necessarily comparable with equivalent statistics retrieved from observables, especially in instances where one hydrometeor species dominates the grid cell and other species are present in trace amounts. A common hydrometeor phase definition must be established to objectively evaluate the phase of simulated hydrometeor populations using observations, which requires the development of a phase classification algorithm that can be applied to observables both forward-simulated and real.

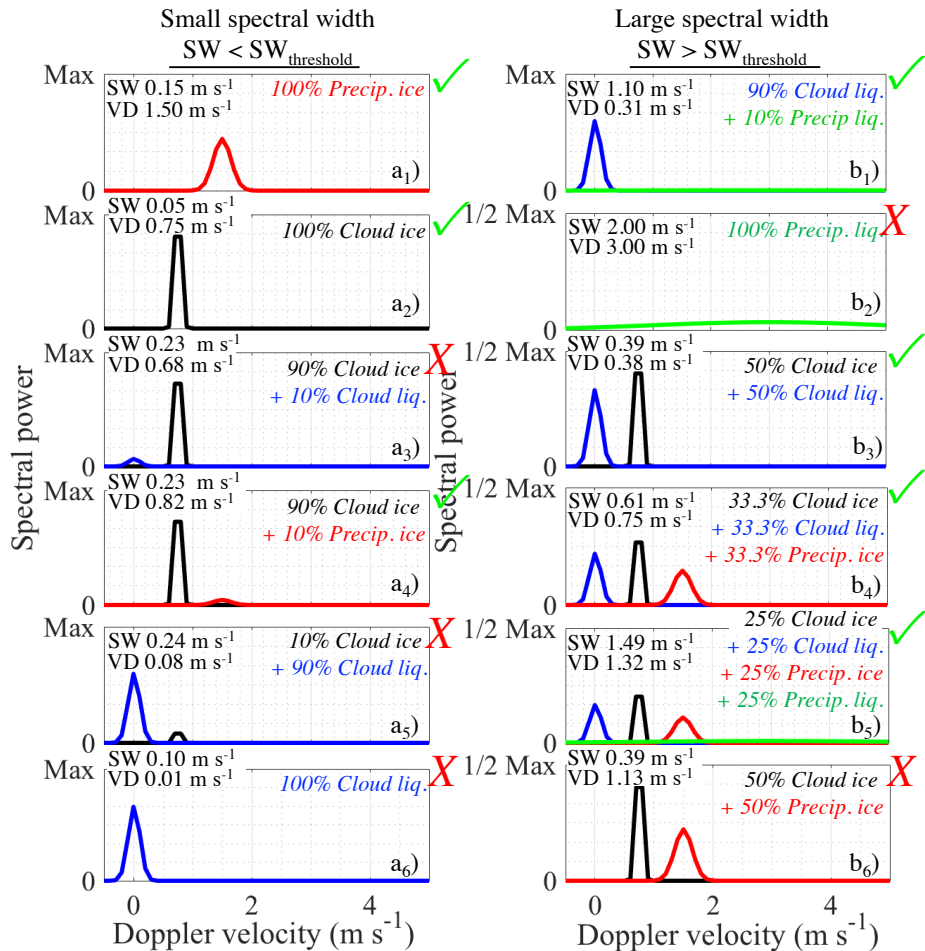
The scientific literature contains a number of phase classification algorithms with different levels of complexity. Hogan et al. (2003) used regions of high lidar backscattered power as an indicator for the presence of liquid droplets. Lidar backscattered power combined with lidar linear depolarization ratio has been used to avoid some of the misclassifications encountered when using backscattered power alone (e.g., Yoshida et al., 2010; Hu et al., 2007a; Hu et al., 2009; Hu et al., 2010; Sassen, 1991). Hogan and O'Connor (2004) proposed using lidar backscattered power in combination with radar reflectivity. While the combination of radar and lidar backscattered powers is useful for the identification of mixed-phase conditions, their combined extent remains limited to single layer clouds or to lower cloud decks because of lidar signal attenuation. Shupe (2007) proposed a technique in which radar Doppler velocity information is used as an alternative to lidar backscattering information (for ranges beyond that of lidar total attenuation) to infer the presence of supercooled water in multi-layer systems. Figure 5 displays cartoons of Doppler spectra that have the same total co-polar radar reflectivity but different total mean Doppler velocities (VD) and Doppler spectral widths (SW) resulting from different hydrometeor species and combinations, thus highlighting the added value of Doppler information. The contribution of each species to the total co-polar reflectivity is indicated as a percentage in the top right of each subpanel. These scenarios show that VD tends to be relatively small for pure liquid cloud (Fig. 5a<sub>6</sub>), pure ice cloud (Fig. 5a<sub>2</sub>), and even mixed-phase non-precipitating cloud (Fig. 5a<sub>3</sub>,a<sub>5</sub>,b<sub>3</sub>) and only tends to increase when precipitation is present in cloud (Fig. 5 a<sub>4</sub>,b<sub>3</sub>,b<sub>4</sub>,b<sub>5</sub>) or below cloud (Fig. 5a<sub>1</sub>,b<sub>2</sub>), making VD a seemingly robust indicator for precipitation occurrence but not for phase identification. These scenarios also show that SW tends to be relatively small in single-phase clouds without precipitation (Fig. 5a<sub>2</sub>,a<sub>6</sub>), pure precipitating ice (Fig. 5a<sub>1</sub>) and multi-species clouds with a dominant hydrometeor species (Fig. 5a<sub>3</sub>,a<sub>5</sub>). On the other hand, SW tends to be large when

**Deleted:** total mean Doppler velocity detected ( $VD_{\text{copol,detect}}$  [ $\text{m s}^{-1}$ ]) is the sum of the reflectivity-weighted contribution of each species. The mass-weighted fall velocity of each species ( $V_{\text{species}}$  [ $\text{m s}^{-1}$ ]) is a GCM output and the:

$$VD_{\text{copol,detect}} = P_{\text{cl}}V_{\text{cl}} + P_{\text{pl}}V_{\text{pl}} + P_{\text{ci}}V_{\text{ci}} + P_{\text{pi}}V_{\text{pi}}. \quad (28)$$

d. Total Doppler spectral width ( $SW_{\text{copol,detect}}$  [ $\text{m s}^{-1}$ ]) is more complex and combines hydrometeor species fall velocity ( $V_{\text{species}}$  [ $\text{m s}^{-1}$ ]) and spectral width ( $SW_{\text{species}}$  [ $\text{m s}^{-1}$ ]) information:

$$SW_{\text{copol,detect}} = P_{\text{cl}} \left( SW_{\text{cl}}^2 + (V_{\text{cl}} - VD_{\text{copol,detect}})^2 \right) + P_{\text{pl}} \left( SW_{\text{pl}}^2 + (V_{\text{pl}} - VD_{\text{copol,detect}})^2 \right) + P_{\text{ci}} \left( SW_{\text{ci}}^2 + (V_{\text{ci}} - VD_{\text{copol,detect}})^2 \right) + P_{\text{pi}} \left( SW_{\text{pi}}^2 + (V_{\text{pi}} - VD_{\text{copol,detect}})^2 \right). \quad (29)$$



613  
614  
615  
616  
617  
618  
619  
620  
621  
622  
623  
624  
625  
626

**Figure 5.** Cartoon examples of radar Doppler spectra from different hydrometeors combinations: precipitating ice (red), cloud ice (black), precipitating water (green) and cloud water (blue). The contribution of each hydrometeor species to the total co-polar reflectivity is indicated in the top right of each subpanel. Each radar Doppler spectrum has been normalized to have the same total co-polar radar reflectivity which highlights that different hydrometeor combinations generate unique mean Doppler velocity (VD) and Doppler spectral width (SW) signatures. As discussed in Sec. 6, low spectral width signatures are assumed to be associated with ice conditions (column a) while high spectral width signatures are assumed to be associated with liquid/mixed-phase conditions (column b). Hydrometeor combinations that respect these assumptions are marked with ✓-marks. Exceptions to these rules (✗-marks) are responsible for (GO)<sup>2</sup>-SIM phase misclassifications above the level of lidar extinction. This list is not exhaustive.

627 liquid precipitation is present (Fig. 5b<sub>1</sub>,b<sub>2</sub>,b<sub>5</sub>) and in mixed-phase clouds without a dominant species (Fig.  
628 5b<sub>3</sub>,b<sub>4</sub>,b<sub>5</sub>). These scenarios suggest that large spectral widths are useful indicators for the presence of  
629 supercooled rain and mixed-phase conditions. Scenarios where this interpretation of spectrum width is  
630 incorrect will be discussed in Sec. 6.3.

631  
632 Regardless of which observation they are based-on, the aforementioned phase classification schemes all  
633 rely on assumption that hydrometeor phases when projected on observational space (e.g., lidar  
634 backscattered power against lidar depolarization ratio) create well-defined patterns that can be separated  
635 using thresholds.

### 636 **6.1 Observational Thresholds for Hydrometeor Phase Identification**

637  
638 While the thresholds used for the radar reflectivity, lidar backscattered power, and lidar  
639 depolarization ratio are generally accepted by the remote sensing community, the same cannot be said  
640 about the radar Doppler velocity and Doppler spectral width thresholds suggested by Shupe (2007).  
641 Because simulated mixing ratios of liquid and ice hydrometeors are known in the (GO)<sup>2</sup>-SIM framework,  
642 the use and choice of all such thresholds for phase classification can be evaluated using joint frequency of  
643 occurrence histograms of hydrometeor mixing ratios for a single species and forward-simulated observable  
644 values (resulting from all hydrometeor types; Fig. 6). This exercise is repeated for each forward-simulation  
645 of the ensemble in order to provide a measure of uncertainty and ensure that the choice of empirical  
646 relationship does not affect our conclusions.

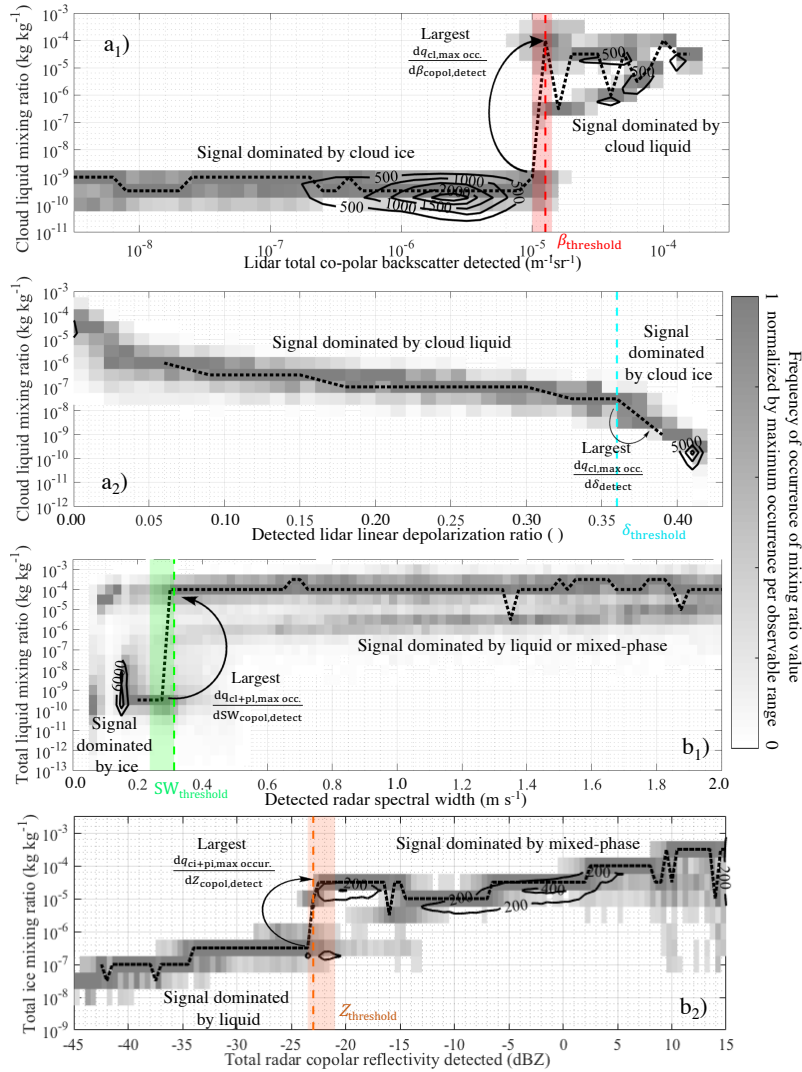
647  
648 As one example, the joint frequency of occurrence histogram of lidar total co-polar backscattered power  
649 ( $\beta_{\text{copol,total,detect}}$ ) and cloud liquid mixing ratio is plotted with the objective of isolating cloud ice particles  
650 from cloud water droplets (Fig. 6a<sub>1</sub>, black contour lines). Two distinct clusters are evident in the joint  
651 histogram in Fig. 6a<sub>1</sub>: 1)  $\beta_{\text{copol,total,detect}}$  between  $10^{-6.7} \text{ m}^{-1}\text{sr}^{-1}$  and  $10^{-5.1} \text{ m}^{-1}\text{sr}^{-1}$  for cloud liquid water  
652 mixing ratios between  $10^{-10.6} \text{ kg kg}^{-1}$  and  $10^{-8.8} \text{ kg kg}^{-1}$  which we conclude result primarily from cloud ice  
653 particle contributions, and 2)  $\beta_{\text{copol,total,detect}}$  between  $10^{-4.6} \text{ m}^{-1}\text{sr}^{-1}$  and  $10^{-3.8} \text{ m}^{-1}\text{sr}^{-1}$  for cloud liquid water  
654 mixing ratios between  $10^{-6.4} \text{ kg kg}^{-1}$  and  $10^{-4.3} \text{ kg kg}^{-1}$  which we conclude result primarily from cloud liquid  
655 droplet contributions. Therefore, a threshold for best distinguishing these two distinct populations should  
656 lie somewhere between  $10^{-5.1} \text{ m}^{-1}\text{sr}^{-1}$  and  $10^{-4.6} \text{ m}^{-1}\text{sr}^{-1}$ .

657  
658 To objectively determine an appropriate threshold to separate different hydrometeor populations, we start  
659 by normalizing the joint histogram of mixing ratio values for fixed ranges of observable values of interest.  
660 This normalization is done by assigning a value of 1 to the frequency of occurrence of the most frequently  
661 occurring mixing ratio value per observable range. It is then possible to evaluate the change of this most  
662 frequently occurring mixing ratio as a function of observable value. The observable value that intersects the  
663 largest change in most frequently occurring mixing ratio is then set as the threshold value.

664  
665 In the example presented in Fig. 6a<sub>1</sub>, the darkest grey shading is indicative of the most frequency occurring  
666 cloud liquid mixing ratio for each lidar backscattered power range. The dotted black line in Fig. 6a<sub>1</sub>  
667 connects these most frequently occurring mixing ratio values. A curved arrow points to the largest change  
668 in most frequently occurring mixing ratio as a function of  $\beta_{\text{copol,total,detect}}$ . A red dashed line at  $10^{-4.9} \text{ m}^{-1}\text{sr}^{-1}$   
669 indicates the lidar backscatter value that intersects this largest change in mixing ratio and represents an  
670 objective threshold value for this example forward-simulation. As mentioned earlier, this threshold is  
671 expected to change with the choice of empirical relationships used in the forward simulator. For the 576  
672 forward-simulator realizations of this version of ModelE outputs, the interquartile range of  $\beta_{\text{copol,total,detect}}$   
673 threshold values ranged from  $10^{-5} \text{ m}^{-1}\text{sr}^{-1}$  to  $10^{-4.85} \text{ m}^{-1}\text{sr}^{-1}$  (red shaded vertical column).

674  
675





676  
 677 **Figure 6.** Example of joint frequency of occurrence histograms (contours) and normalized subsets from the  
 678 joint histograms (grey shading) for one (GO)<sup>2</sup>-SIM forward-realization: a<sub>1</sub>)  $\beta_{\text{copol,total,detect}}$ , a<sub>2</sub>)  $\delta_{\text{detect}}$ , b<sub>1</sub>)  
 679  $SW_{\text{copol,detect}}$ , and b<sub>2</sub>)  $Z_{\text{copol,total,detect}}$ . These are used for the determination of objective water phase  
 680 classifier thresholds (vertical colored dashed lines) that are set at the observational value with the largest  
 681 change (see curved arrows) in most frequently occurring mixing ratio. These thresholds are not fixed but  
 682 rather re-estimated for each forward-ensemble member. The widths of the color shaded vertical columns  
 683 represent the interquartile range spreads generated from 576 different forward-realizations.  
 684

685 The different panels in Fig. 6 show that similar observational patterns occur in the water mixing ratio  
686 versus lidar or radar observable histograms such that objective thresholds for hydrometeor phase  
687 classification can be determined for all of them. The second threshold determined is for the detected lidar  
688 linear depolarization ( $\delta_{\text{detect}}$ ), once again with the goal of separating returns dominated by cloud droplets  
689 versus cloud ice particles (Fig. 6a<sub>2</sub>). If we first identify the model grid cells with backscattered power above  
690 the lidar detectability threshold of  $10^{-6} \text{ m}^{-1} \text{ sr}^{-1}$ , the threshold to distinguish between ice particles and liquid  
691 droplets is 0.36 (cyan dashed line). In the 576 forward realizations from this version of ModelE this  
692 threshold is stable at 0.36. Note that this threshold is not allowed to fall below  $0.05 \text{ m s}^{-1}$ .

693  
694 The third threshold determined is the radar detected co-polar spectral width ( $\text{SW}_{\text{copol,detect}}$ ) value that  
695 separates ice dominated from liquid/mixed-phase dominated returns (Fig. 6b<sub>1</sub>). We isolate the model grid  
696 cells with sub-zero temperatures and look for the most appropriate  $\text{SW}_{\text{copol,detect}}$  threshold between  $0.2 \text{ m s}^{-1}$   
697 and  $0.5 \text{ m s}^{-1}$  to isolate the ice population. For the example forward-simulation we find a threshold of  $0.31$   
698  $\text{m s}^{-1}$  (green dashed line), and over all forward-realizations this threshold ranges from  $0.24 \text{ m s}^{-1}$  to  $0.31 \text{ m}$   
699  $\text{s}^{-1}$  (green shaded vertical column).

700  
701 The last threshold determined is the radar total co-polar reflectivity detected ( $Z_{\text{copol,total,detect}}$ ) value that  
702 separates liquid from mixed-phase dominated returns (Fig. 6b<sub>2</sub>). If we isolate the model grid cells with sub-  
703 zero temperatures, spectral widths within the liquid/mixed-phase range, and with mean Doppler velocities  
704 smaller than  $1 \text{ m s}^{-1}$ , the threshold to distinguish between liquid and mixed-phase is objectively set to  $-23$   
705 dBZ (orange dashed line). This threshold ranges from  $-23.5 \text{ dBZ}$  to  $-21.0 \text{ dBZ}$  over the 576 forward  
706 realizations obtained from this version of ModelE outputs (orange shaded vertical column).

707  
708 The objectively determined thresholds, [based on model output mixing ratios](#), optimize the performance of  
709 the hydrometeor phase classification algorithm and are expected to generate the best (by minimizing false  
710 detection) hydrometeor phase classifications. Results using these [objective flexible](#) thresholds are  
711 compared in Sec. 6.4 to results using the fixed empirical thresholds of Shupe (2007).

Deleted: flexible

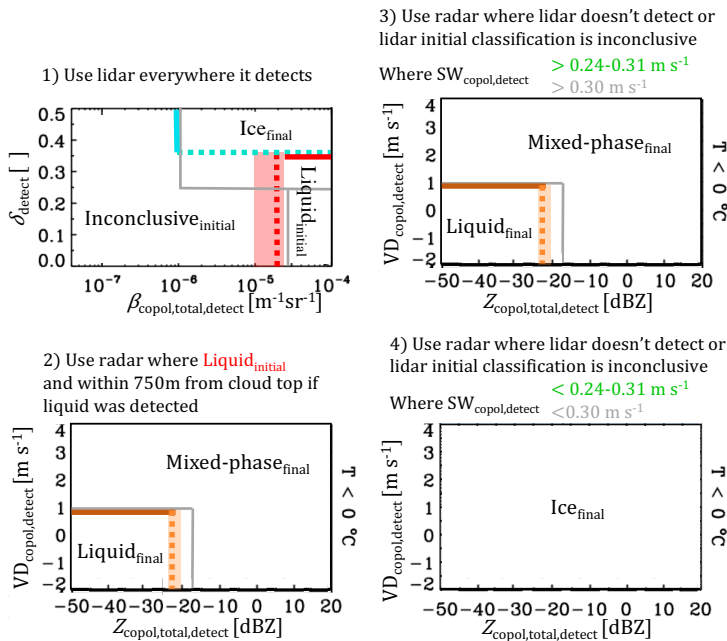
Deleted: 3

## 713 6.2 Hydrometeor Phase Map Generation

714  
715 Hydrometeor phase maps are produced for each forward realization by applying the objectively  
716 determined flexible thresholds or fixed [empirical](#) thresholds modified from Shupe (2007) as illustrated in  
717 Fig. 7.

718  
719 Thresholds are applied in sequence. Where the lidar signal is detected it is used for initial classification of  
720 liquid-dominated grid cells (Fig. 7.1, red box) and final classification of ice-dominated grid cells (Fig. 7.1,  
721 cyan box). Grid cells initially classified as containing liquid drops by the lidar are subsequently reclassified  
722 as either liquid dominated (Fig. 7.2, orange box) or mixed-phase (Fig. 7.2, outside of orange box) by the  
723 radar which is more sensitive to the larger ice particles. Because studies suggest that supercooled water  
724 layers extend to the tops of shallow clouds, if liquid containing grid cells were identified within 750 m of  
725 cloud top, the radar is used to determine if there are other liquid or mixed-phase hydrometeor populations  
726 from the range of lidar attenuation to cloud top (Fig.7.2; and just as in Shupe (2007)). Hydrometeor-  
727 containing grid cells either not detected by the lidar or whose initial phase classification is inconclusive  
728 (Fig. 7.1, inconclusive region) are subsequently classified using their radar moments. If radar spectral width  
729 is above the threshold grid cells are finally classified as liquid (Fig.7.3, orange box) or mixed-phase (Fig.  
730 7.3, outside the orange box) depending on their other radar moments. If radar spectral width is below the  
731 threshold grid cells are finally classified as ice phase (Fig. 7.4). As a final step detected hydrometeors in  
732 grid cells at temperatures above  $0 \text{ }^\circ\text{C}$  are reclassified to liquid phase while those at temperatures below  $-40$   
733  $^\circ\text{C}$  are reclassified to the ice phase.

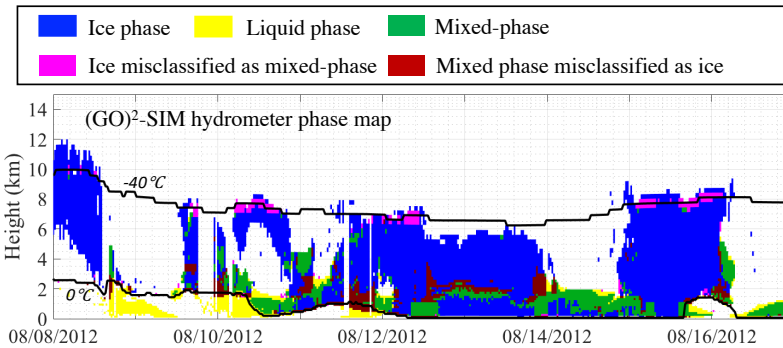
734



738  
739  
740  
741  
742  
743  
744

**Figure 7.** Collective illustration of hydrometeor phase classification thresholds and phase classification sequence. Fixed empirical thresholds modified from Shupe (2007) are displayed as grey lines. The objectively determined flexible thresholds are displayed using dashed colored lines and colored shading as in Fig. 6. Note that positive velocities indicate downward motion.

745 Figure 8 shows an example of (GO)<sup>2</sup>-SIM water phase classification for one forward-ensemble member  
746 using objectively determined thresholds. During the first day of this example simulation, ModelE produced  
747 what appears to be a thick cirrus. The simulator classified this cirrus as mostly ice phase (blue). The  
748 following day of 08/09, ModelE generated enough hydrometeors to attenuate both the forward-simulated  
749 lidar and radar signals. The algorithm identified these hydrometeors as liquid phase (yellow). For the  
750 following few days (08/11-08/14) deep hydrometeor systems extending from the surface to about 8 km  
751 were produced. According to (GO)<sup>2</sup>-SIM they were mostly made up of ice-phase particles (blue) with two  
752 to three shallow mixed-phase layers at 2 km, 4 km and 7 km. Finally, on 08/14 hydrometeor systems appear  
753 to become shallower (2-km altitudes) and liquid topped (yellow). For the entire one-year simulation, of the  
754 333,927 detectable hydrometeor-containing grid cells, the phase classifier applied to our example forward-  
755 simulation ensemble member identified 12.2 % pure-liquid, 68.7 % pure-ice and 19.1 % mixed-phase  
756 conditions. Hydrometeor phase statistics estimated using this objective definition of hydrometeor phase  
757 differ by up to 60 % from those discussed at the beginning of this section that were simply based on model  
758 output nonzero mixing ratios. This indicates that a large number of grid cells containing detectable  
759 hydrometeor populations were dominated by one species and that the amounts of the other species were too  
760 small to create a phase classification signal. This highlights the need to create a framework that both  
761 objectively identifies grid cells containing detectable hydrometeors populations and determines the phase  
762 of the hydrometeors dominating them using a phase classification technique consistent with observations.



763  
764  
765  
766  
767  
768  
769  
770  
771  
772

**Figure 8.** Example output from (GO)<sup>2</sup>-SIM phase-classification algorithms (using objectively determined thresholds and one set of empirical relationships in the forward-simulator). The locations of ice-phase hydrometeors (blue), liquid-phase hydrometeors (yellow) and mixed-phase hydrometeors (green) are illustrated. After evaluation against the original ModelE output mixing-ratios, we found that some mixed-phase hydrometeors were misclassified as ice phase (red) and some ice-phase hydrometeors were misclassified as mixed phase (magenta). Also indicated are the locations of the 0 °C and -40 °C isotherms (black lines).

773  
774

### 6.3 Phase Classification Algorithm Limitations

775  
776  
777  
778  
779

Hydrometer-phase classification evaluation is facilitated in the context of forward-simulators because inputs (i.e., model-defined hydrometer phase) are known. Model mixing-ratios are used to check for incorrect hydrometer phase classifications over the entire forward-realization ensemble (Table 1b).

780  
781  
782  
783  
784  
785  
786  
787  
788  
789  
790

Without any ambiguity, it is possible to identify false-positive phase classifications (Table 1b). A false-positive phase classification occurs when a grid cell containing 0 kg kg<sup>-1</sup> of ice particles (liquid drops) is wrongly classified as ice or mixed phase (liquid or mixed phase). In this study a negligible number (0.5 %) of hydrometer-containing model grid cells are wrongly classified as containing liquid. Similarly, a negligible number (~0.0 %) of hydrometer-containing model grid cells are wrongly classified as containing ice particles, whereas 1.1 % of pure liquid- or ice-containing model grid cells are wrongly classified as mixed-phase. Using model mixing ratios, it is possible to determine the appropriate phase of these false-positive classifications (“False negative” row in Table 1b). An additional 1.5 % of all hydrometer-containing model grid cells should be classified as ice phase while a negligible number (0.2 %) of liquid water is missed.

791  
792  
793  
794  
795  
796  
797  
798

Quantifying the number of mixed-phase false negatives (i.e., the number of grid cells that should have been, but were not, classified as mixed-phase) is not as straightforward because it requires us to define mixed-phase conditions in model space. For a rough estimate of mixed-phase false negatives we check if model grid cells classified as containing a single phase contained large amounts of hydrometeors of other phase types, with large amount being defined here as a mixing-ratio greater than 10<sup>-5</sup> kg kg<sup>-1</sup>. This mixing-ratio amount was chosen because it is associated with noticeable changes in observables, as seen in Fig. 6. Using this mixed-phase definition, we find that 1.4 % of liquid-only classified grid cells contained large amounts of ice particles and 3.8 % of ice-only classified grid cells contained large amounts of liquid

799 (“Questionable” row in Table 1b). Everything considered, only 6.9 % of model grid cells with detectable  
800 hydrometeor populations were misclassified according to their phase.

801

802 For completeness we examined the circumstances associated with the most frequent phase-classification  
803 errors. Most of these errors occurred above the altitude at which the lidar beam was completely attenuated,  
804 where only radar spectral widths are used to separate liquid/mixed-phase hydrometeors from ice-phase  
805 hydrometeors.

806

807 The first set of phase-classifier errors was a scarcity of pure ice particles (1.5 % false-negative ice phase).  
808 In the current (GO)<sup>2</sup>-SIM implementation, ice particle populations are sometimes incorrectly classified as  
809 liquid/mixed-phase populations where cloud ice and precipitating ice hydrometeors coexist. This happens  
810 because mixtures of cloud and precipitating ice particles sometimes generate large Doppler spectral widths  
811 similar to those of mixed-phase clouds (Fig. 5b<sub>6</sub>). In this example simulation ModelE produced such  
812 mixtures close to the -40 °C isotherm near the tops of deep cloud systems (e.g., Fig. 8, 08/15 around 8 km;  
813 magenta).

814

815 In contrast, mixed-phase conditions were sometimes misclassified as pure ice (3.8 %; “Questionable” row  
816 in Table 1b). This occurred when large amounts of liquid drops coexisted with small amounts of ice  
817 particles that generated small spectral widths incorrectly associated with pure ice particles (Fig. 5a<sub>5</sub>). In this  
818 example simulation, ModelE produced such conditions just above the altitude of lidar beam extinction in  
819 cloud layers with ice falling into supercooled water layers (e.g., Fig. 8, 08/13 around 3 km; red).

820

821 Other possible misclassification scenarios associated with spectral width retrievals are presented in Fig. 5  
822 and identified with the red X-marks. These other misclassification scenarios are not responsible for large  
823 misclassification errors here but could be in other simulations. As such, (GO)<sup>2</sup>-SIM errors should be  
824 quantified every time it is applied to a new region or numerical model.

825

#### 826 6.4 Sensitivity on the Choice of Threshold

827

828 The performance of the objectively determined flexible phase-classification thresholds (illustrated  
829 using colored dashed lines and shading in Fig. 7) is examined against those empirically derived by Shupe  
830 (2007) with one exception (illustrated using grey lines in Fig. 7). The modification to Shupe (2007) is that  
831 radar reflectivity larger than 5 dBZ are not associated with the snow category since introducing this  
832 assumption was found to increase hydrometeor-phase misclassification (not shown). From Fig. 7 it is  
833 apparent that both sets of thresholds are very similar. We estimate that hydrometeor phase frequency of  
834 occurrence produced by both threshold sets are within 6.1 % of each other and that the fixed empirical  
835 thresholds modified from Shupe (2007) only produce phase misclassification in an additional 0.7 % of  
836 hydrometeor-containing grid cells (compare Table 1b to Table 1c). These results suggest that the use of  
837 lidar-radar threshold-based techniques for hydrometeor-phase classification depends little on the choice of  
838 thresholds.

839

#### 840 7 An Ensemble Approach for Uncertainty Quantification

841

842 Owing to the limited information content in models with regard to detailed particle property  
843 information, all forward simulators must rely on a set of assumptions to estimate hydrometeor  
844 backscattered power. (GO)<sup>2</sup>-SIM performs an uncertainty assessment by performing an ensemble of 576  
845 forward simulations based on 18 different empirical relationships (relationships are listed in Table 2).  
846 While the relationships used do not cover the entire range of possible backscattering assumptions, they  
847 represent an attempt at uncertainty quantification and illustrate a framework for doing so. We express the  
848 spread generated by the different empirical relationships combinations using median values and

Deleted: proposed

Deleted: T

Deleted: sc

Deleted: is expressed

853 interquartile ranges (IQR; Table 1b,c). The fact that the largest interquartile range is 3.7 % suggests that the  
854 number of grid cells containing detectable hydrometeors as well as hydrometeor phase statistics estimated  
855 using the proposed lidar-radar algorithm are rather independent of backscattered power assumptions in the  
856 forward simulator. Nevertheless, we suggest using the full range of frequency of occurrences presented in  
857 Tables 1b,c for future model evaluation using observations and acknowledge that additional uncertainty is  
858 most likely present.

Deleted: .  
Formatted: Font: (Default) Times New Roman

## 860 8 Summary and Conclusions

861  
862 Ground-based active remote sensors offer a favorable perspective for the study of shallow and  
863 multi-layer mixed-phase clouds because ground-based sensors are able to collect high resolution  
864 observations close to the surface where supercooled water layers are expected to be found. In addition,  
865 ground-based sensors have the unique capability to collect Doppler velocity information that has the  
866 potential to help identify mixed-phase conditions even in multi-layer cloud systems.

867  
868 Because of differences in hydrometeor and phase definitions, among other things, observations remain  
869 incomplete benchmarks for general circulation model (GCM) evaluation. Here, a GCM-oriented ground-  
870 based observation forward-simulator [(GO)<sup>2</sup>-SIM] framework for hydrometeor-phase evaluation is  
871 presented. This framework bridges the gap between observations and GCMs by mimicking observations  
872 and their limitations and producing hydrometeor-phase maps with comparable hydrometeor definitions and  
873 uncertainties.

874  
875 Here, results over the North Slope of Alaska extracted from a one-year global ModelE (current  
876 development version) simulation are used as an example. (GO)<sup>2</sup>-SIM uses as input native resolution GCM  
877 grid-average hydrometeor (cloud and precipitation, liquid and ice) area fractions, mixing ratios, mass-  
878 weighted fall speeds and effective radii. These variables offer a balance between those most essential for  
879 forward simulation of observed hydrometeor backscattering and those likely to be available from a range of  
880 GCMs going forward, making (GO)<sup>2</sup>-SIM a portable tool for model evaluation. (GO)<sup>2</sup>-SIM outputs  
881 statistics from 576 forward-simulation ensemble members all based on a different combination of eighteen  
882 empirical relationships that relate simulated water content to hydrometeor backscattered power as would be  
883 observed by vertically pointing micropulse lidar and Ka-band radar; The interquartile range of these  
884 statistics being used as an uncertainty measure.

885  
886 (GO)<sup>2</sup>-SIM objectively determines which hydrometeor-containing model grid cells can be assessed based  
887 on sensor capabilities, bypassing the need to arbitrarily filter trace amounts of simulated hydrometeor  
888 mixing ratios that may be unphysical or just numerical noise. Limitations that affect sensor capabilities  
889 represented in (GO)<sup>2</sup>-SIM include attenuation and range dependent sensitivity. In this approach 78.3 % of  
890 simulated grid cells containing nonzero hydrometeor mixing ratios were detectable and can be evaluated  
891 using real observations, with the rest falling below the detection capability of the forward-simulated lidar  
892 and radar leaving them unevaluated. This shows that comparing all hydrometeors produced by models with  
893 those detected by sensors would lead to inconsistencies in the evaluation of quantities as simple as cloud  
894 and precipitation locations and fraction.

895  
896 While information can be gained from comparing the forward-simulated and observed fields, hydrometeor-  
897 phase evaluation remains challenging owing to inconsistencies in hydrometeor-phase definitions. Models  
898 evolve ice and liquid water species separately such that their frequency of occurrence can easily be  
899 estimated. However, sensors record information from all hydrometeor species within a grid cell without  
900 distinction between signals originating from ice particles or liquid drops. The additional observables of  
901 lidar linear depolarization ratio and radar mean Doppler velocity and spectral width are forward simulated  
902 to retrieve hydrometeor phase. The results presented here strengthen the idea that hydrometeor-phase

904 characteristics lead to distinct signatures in lidar and radar observables, including the radar Doppler  
905 moments which have not been evaluated previously. Our analysis confirms that distinct patterns in  
906 observational space are related to hydrometeor phase and an objective technique to isolate liquid, mixed-  
907 phase and ice conditions using simulated hydrometeor mixing ratios was presented. The thresholds  
908 produced by this technique are close to those previously estimated using real observations, further  
909 highlighting the robustness of thresholds for hydrometeor-phase classification.

910  
911 The algorithm led to hydrometeor phase misclassification in no more than 6.9 % of the hydrometeor-  
912 containing grid cells. Its main limitations were confined above the altitude of lidar total attenuation where it  
913 sometimes failed to identify additional mixed-phase layers dominated by liquid water drops and with few  
914 ice particles. Using the same hydrometeor-phase definition for forward-simulated observables and real  
915 observations should produce hydrometeor-phase statistics with comparable uncertainties. Alternatively,  
916 disregarding how hydrometeor phase is observationally retrieved would lead to discrepancies in  
917 hydrometeor-phase frequency of occurrence up to 40 %, a difference attributable to methodological bias  
918 and not to model error. So, while not equivalent to model “reality” a forward-simulator framework offers  
919 the opportunity to compare simulated and observed hydrometeor-phase maps with similar limitations and  
920 uncertainties for a fair model evaluation.

921  
922 The next steps to GCM evaluation using ground-based observations include the creation of an artifact-free  
923 observational benchmark and addressing model and observation scale differences. While the (GO)<sup>2</sup>-SIM  
924 modules presented here capture sensor limitations related to backscattered power attenuations, they do not  
925 account for sensitivity inconsistencies, clutter and insect contamination, all of which affect the observations  
926 collected by the real sensors. Only thorough evaluation of observational datasets and application of  
927 masking algorithms to them can remediate these issues. Several approaches, from the subsampling of  
928 GCMs to the creation of CFADs, have been proposed to address the scale difference. A follow-up study  
929 will describe an approach by which vertical and temporal resampling of observations can help reduce the  
930 scale gap. Furthermore, it will be showed that, using simplified model evaluation targets based on three  
931 atmospheric regions separated by constant pressure levels, ground-based observations can be used for  
932 GCM hydrometeor-phase evaluation.

933  
934 (GO)<sup>2</sup>-SIM is a step towards creating a fair hydrometeor-phase comparison between GCM output and  
935 ground-based observations. Owing to its simplicity and robustness, (GO)<sup>2</sup>-SIM is expected to help assist in  
936 model evaluation and development for models such as ModelE, specifically with respect to hydrometeor  
937 phase in shallow cloud systems.

### 938 939 Code Availability

940  
941 Results here are based on ModelE tag modelE3\_2017-06-14, which is not a publicly released  
942 version of ModelE but is available on the ModelE developer repository  
943 at [https://simplex.giss.nasa.gov/cgi-bin/gitweb.cgi?p=modelE.git;a=tag;h=refs/tags/modelE3\\_2017-06-14](https://simplex.giss.nasa.gov/cgi-bin/gitweb.cgi?p=modelE.git;a=tag;h=refs/tags/modelE3_2017-06-14).  
944 The (GO)<sup>2</sup>-SIM modules described in the current manuscript can be fully reproduced using the information  
945 provided. Interested parties are encouraged to contact the corresponding author for additional information  
946 on how to interface their numerical model with (GO)<sup>2</sup>-SIM.

### 947 948 Acknowledgements

949  
950 K. Lamer and E. Clothiaux’s contributions to this research were funded by subcontract 300324 of  
951 the Pennsylvania State University with the Brookhaven National Laboratory in support to the ARM-ASR  
952 Radar Science group. The contributions of A. Fridlind, A. Ackerman, and M. Kelley were partially  
953 supported by the Office of Science (BER), U.S. Department of Energy, under agreement DE-SC0016237,

Deleted: will describe how

Deleted: observational resampling in the context of the cloud vertical structure approach (Rémillard and Tselioudis, 2015) can be used to account for scale differences in the context of GCM hydrometeor-phase evaluation. ¶

Deleted: The ModelE code used to produce the results presented here resides within the ModelE development repository and is available upon request from the corresponding author.

963 the NASA Radiation Sciences Program, and the NASA Modeling, Analysis and Prediction Program.  
964 Resources supporting this work were provided by the NASA High-End Computing (HEC) Program  
965 through the NASA Center for Climate Simulation (NCCS) at Goddard Space Flight Center.  
966

## 967 **References**

- 968 Atlas, D.: The estimation of cloud parameters by radar, *J. Meteorol.*, 11, 309-317, 1954.
- 970 Atlas, D., Matrosov, S. Y., Heymsfield, A. J., Chou, M.-D., and Wolff, D. B.: Radar and radiation  
971 properties of ice clouds, *J. Appl. Meteorol.*, 34, 2329-2345, 1995.
- 972 Battaglia, A., and Delanoë, J.: Synergies and complementarities of CloudSat-CALIPSO snow  
973 observations, *J. Geophys. Res.: Atmos.*, 118, 721-731, 2013.
- 974 Battan, L. J.: Radar observation of the atmosphere, University of Chicago, Chicago, Illinois, 1973.
- 975 Bodas-Salcedo, A., Webb, M., Bony, S., Chepfer, H., Dufresne, J.-L., Klein, S., Zhang, Y.,  
976 Marchand, R., Haynes, J., and Pincus, R.: COSP: Satellite simulation software for model assessment, *Bull.*  
977 *Amer. Meteorol. Soc.*, 92, 1023-1043, 2011.
- 978 Bretherton, C. S., and Park, S.: A new moist turbulence parameterization in the Community  
979 Atmosphere Model, *J. Climate*, 22, 3422-3448, 2009.
- 980 Cesana, G., and Chepfer, H.: Evaluation of the cloud thermodynamic phase in a climate model  
981 using CALIPSO-GOCCP, *J. Geophys. Res.: Atmos.*, 118, 7922-7937, 2013.
- 982 Chepfer, H., Bony, S., Winker, D., Chiriaco, M., Dufresne, J. L., and Sèze, G.: Use of CALIPSO  
983 lidar observations to evaluate the cloudiness simulated by a climate model, *Geophys. Res. Lett.*, 35, 2008.
- 984 de Boer, G., Eloranta, E. W., and Shupe, M. D.: Arctic mixed-phase stratiform cloud properties  
985 from multiple years of surface-based measurements at two high-latitude locations, *J. Atmos. Sci.*, 66, 2874-  
986 2887, 2009.
- 987 Dong, X., and Mace, G. G.: Arctic stratus cloud properties and radiative forcing derived from  
988 ground-based data collected at Barrow, Alaska, *J. climate*, 16, 445-461, 2003.
- 989 [Ellis, S. M., and Vivekanandan, J.: Liquid water content estimates using simultaneous S and Ka  
990 band radar measurements, \*Radio Science\*, 46, 2011.](#)
- 991 English, J. M., Kay, J. E., Gettelman, A., Liu, X., Wang, Y., Zhang, Y., and Chepfer, H.:  
992 Contributions of clouds, surface albedos, and mixed-phase ice nucleation schemes to Arctic radiation biases  
993 in CAM5, *J. Climate*, 27, 5174-5197, 2014.
- 995 [Everitt, B., and Hand, D.: Mixtures of normal distributions, in: \*Finite Mixture Distributions\*,  
996 \*Springer\*, 25-57, 1981.](#)
- 997 Fox, N. I., and Illingworth, A. J.: The retrieval of stratocumulus cloud properties by ground-based  
998 cloud radar, *J. Appl. Meteorol.*, 36, 485-492, 1997.
- 1000 Frey, W., Maroon, E., Pendergrass, A., and Kay, J.: Do Southern Ocean Cloud Feedbacks Matter  
1001 for 21st Century Warming?, *Geophys. Res. Lett.*, 2017.



1002 Gattelman, A., and Morrison, H.: Advanced two-moment bulk microphysics for global models. Part  
1003 I: Off-line tests and comparison with other schemes, *J. Climate*, 28, 1268-1287, 2015.

1004 Gattelman, A., Morrison, H., Santos, S., Bogenschutz, P., and Caldwell, P.: Advanced two-moment  
1005 bulk microphysics for global models. Part II: Global model solutions and aerosol–cloud interactions, *J.*  
1006 *Climate*, 28, 1288-1307, 2015.

1007 Hagen, M., and Yuter, S. E.: Relations between radar reflectivity, liquid-water content, and rainfall  
1008 rate during the MAP SOP, *Quart. J. Roy. Meteorol. Soc.*, 129, 477-493, 2003.

1009 Haynes, J., Luo, Z., Stephens, G., Marchand, R., and Bodas-Salcedo, A.: A multipurpose radar  
1010 simulation package: QuickBeam, *Bull. Amer. Meteorol. Soc.*, 88, 1723-1727, 2007.

1011 Heymsfield, A., Winker, D., Avery, M., Vaughan, M., Diskin, G., Deng, M., Mitev, V., and  
1012 Matthey, R.: Relationships between ice water content and volume extinction coefficient from in situ  
1013 observations for temperatures from 0 to– 86° C: Implications for spaceborne lidar retrievals, *J. Appl.*  
1014 *Meteorol. Climatol.*, 53, 479-505, 2014.

1015 Heymsfield, A. J., Winker, D., and van Zadelhoff, G. J.: Extinction-ice water content-effective  
1016 radius algorithms for CALIPSO, *Geophys. Res. Lett.*, 32, 2005.

1017 Hogan, R. J., Illingworth, A., O'connor, E., and Baptista, J.: Characteristics of mixed-phase clouds.  
1018 II: A climatology from ground-based lidar, *Quart. J. Roy. Meteorol. Soc.*, 129, 2117-2134, 2003.

1019 Hogan, R. J., Behera, M. D., O'Connor, E. J., and Illingworth, A. J.: Estimate of the global  
1020 distribution of stratiform supercooled liquid water clouds using the LITE lidar, *Geophys. Res. Lett.*, 31,  
1021 2004.

1022 Hogan, R. J., and O'Connor, E.: Facilitating cloud radar and lidar algorithms: The Cloudnet  
1023 Instrument Synergy/Target Categorization product, Cloudnet documentation, 2004.

1024 Hogan, R. J., Mittermaier, M. P., and Illingworth, A. J.: The retrieval of ice water content from  
1025 radar reflectivity factor and temperature and its use in evaluating a mesoscale model, *J. Appl. Meteorol.*  
1026 *Climatol.*, 45, 301-317, 2006.

1027 Hu, Y., Vaughan, M., Liu, Z., Lin, B., Yang, P., Flittner, D., Hunt, B., Kuehn, R., Huang, J., and  
1028 Wu, D.: The depolarization-attenuated backscatter relation: CALIPSO lidar measurements vs. theory,  
1029 *Optics Express*, 15, 5327-5332, 2007a.

1030 Hu, Y., Vaughan, M., McClain, C., Behrenfeld, M., Maring, H., Anderson, D., Sun-Mack, S.,  
1031 Flittner, D., Huang, J., Wielicki, B., Minnis, P., Weimer, C., Trepte, C., and Kuehn, R.: Global statistics of  
1032 liquid water content and effective number concentration of water clouds over ocean derived from  
1033 combined CALIPSO and MODIS measurements, *Atmos. Chem. Phys.*, 7, 3353–3359, 10.5194/acp-7-  
1034 3353-2007, 2007b.

1035 Hu, Y., Winker, D., Vaughan, M., Lin, B., Omar, A., Trepte, C., Flittner, D., Yang, P., Nasiri, S. L.,  
1036 and Baum, B.: CALIPSO/CALIOP cloud phase discrimination algorithm, *J. Atmos. Ocean. Technol.*, 26,  
1037 2293-2309, 2009.

1038 Hu, Y., Rodier, S., Xu, K. m., Sun, W., Huang, J., Lin, B., Zhai, P., and Josset, D.: Occurrence,  
1039 liquid water content, and fraction of supercooled water clouds from combined CALIOP/IIR/MODIS  
1040 measurements, *J. Geophys. Res.: Atmos.*, 115, 2010.

1041 Huang, Y., Siems, S. T., Manton, M. J., Hande, L. B., and Haynes, J. M.: The structure of low-  
1042 altitude clouds over the Southern Ocean as seen by CloudSat, *J. Climate*, 25, 2535-2546, 2012a.

1043 Huang, Y., Siems, S. T., Manton, M. J., Protat, A., and Delanoë, J.: A study on the low-altitude  
1044 clouds over the Southern Ocean using the DARDAR-MASK, *J. Geophys. Res.: Atmos.*, 117, 2012b.

1045 Intrieri, J., Shupe, M., Uttal, T., and McCarty, B.: An annual cycle of Arctic cloud characteristics  
1046 observed by radar and lidar at SHEBA, *J. Geophys. Res.: Oceans*, 107, 2002.

1047 Kalesse, H., Szyrmer, W., Kneifel, S., Kollias, P., and Luke, E.: Fingerprints of a riming event on  
1048 cloud radar Doppler spectra: observations and modeling, *Atmos. Chem. Phys.*, 16, 2997-3012, 2016.

1049 Kay, J. E., Bourdages, L., Miller, N. B., Morrison, A., Yettella, V., Chepfer, H., and Eaton, B.:  
1050 Evaluating and improving cloud phase in the Community Atmosphere Model version 5 using spaceborne  
1051 lidar observations, *J. Geophys. Res.: Atmos.*, 121, 4162-4176, 2016.

1052 Kikuchi, K., Tsuboya, S., Sato, N., Asuma, Y., Takeda, T., and Fujiyoshi, Y.: Observation of  
1053 wintertime clouds and precipitation in the Arctic Canada (POLEX-North), *J. Meteorol. Soc. Japan. Ser. II*,  
1054 60, 1215-1226, 1982.

1055 Klein, S. A., McCoy, R. B., Morrison, H., Ackerman, A. S., Avramov, A., Boer, G. d., Chen, M.,  
1056 Cole, J. N., Del Genio, A. D., and Falk, M.: Intercomparison of model simulations of mixed-phase clouds  
1057 observed during the ARM Mixed-Phase Arctic Cloud Experiment. I: Single-layer cloud, *Quart. J. Roy.  
1058 Meteorol. Soc.*, 135, 979-1002, 2009.

1059 Kollias, P., Miller, M. A., Luke, E. P., Johnson, K. L., Clothiaux, E. E., Moran, K. P., Widener, K.  
1060 B., and Albrecht, B. A.: The Atmospheric Radiation Measurement Program cloud profiling radars: Second-  
1061 generation sampling strategies, processing, and cloud data products, *J. Atmos. Ocean. Technol.*, 24, 1199-  
1062 1214, 2007.

1063 Kollias, P., Rémillard, J., Luke, E., and Szyrmer, W.: Cloud radar Doppler spectra in drizzling  
1064 stratiform clouds: 1. Forward modeling and remote sensing applications, *J. Geophys. Res.: Atmos.*, 116,  
1065 2011.

1066 Kollias, P., Clothiaux, E. E., Ackerman, T. P., Albrecht, B. A., Widener, K. B., Moran, K. P., Luke,  
1067 E. P., Johnson, K. L., Bharadwaj, N., and Mead, J. B.: Development and applications of ARM millimeter-  
1068 wavelength cloud radars, *Meteorological Monographs*, 57, 17.11-17.19, 2016.

1069 Kuehn, R., Holz, R., Eloranta, E., Vaughan, M., and Hair, J.: Developing a Climatology of Cirrus  
1070 Lidar Ratios Using University of Wisconsin HSRL Observations, *EPJ Web of Conferences*, 2016, 16009,

1071 Liao, L., and Sassen, K.: Investigation of relationships between Ka-band radar reflectivity and ice  
1072 and liquid water contents, *Atmospheric Res.*, 34, 231-248, 1994.

1073 Liu, C.-L., and Illingworth, A. J.: Toward more accurate retrievals of ice water content from radar  
1074 measurements of clouds, *J. Appl. Meteorol.*, 39, 1130-1146, 2000.

1075 McCoy, D. T., Tan, I., Hartmann, D. L., Zelinka, M. D., and Storelvmo, T.: On the relationships  
1076 among cloud cover, mixed-phase partitioning, and planetary albedo in GCMs, *J. Advances in Modeling  
1077 Earth Systems*, 8, 650-668, 2016.

l078 O'Connor, E. J., Illingworth, A. J., and Hogan, R. J.: A technique for autocalibration of cloud lidar,  
l079 J. Atmos. Ocean. Technol., 21, 777-786, 2004.

l080 Rémillard, J., and Tselioudis, G.: Cloud regime variability over the Azores and its application to  
l081 climate model evaluation, J. Climate, 28, 9707-9720, 2015.

l082 Sassen, K.: Ice cloud content from radar reflectivity, J. climate and Appl. Meteorol., 26, 1050-1053,  
l083 1987.

l084 Sassen, K.: The polarization lidar technique for cloud research: A review and current assessment,  
l085 Bull. Amer. Meteorol. Soc., 72, 1848-1866, 1991.

l086 Sato, N., Kikuchi, K., Barnard, S. C., and Hogan, A. W.: Some characteristic properties of ice  
l087 crystal precipitation in the summer season at South Pole Station, Antarctica, J. Meteorol. Soc. Japan. Ser.  
l088 II, 59, 772-780, 1981.

l089 Sauvageot, H., and Omar, J.: Radar reflectivity of cumulus clouds, J. Atmos. Ocean. Technol., 4,  
l090 264-272, 1987.

l091 Schmidt, G. A., Kelley, M., Nazarenko, L., Ruedy, R., Russell, G. L., Aleinov, I., Bauer, M., Bauer,  
l092 S. E., Bhat, M. K., and Bleck, R.: Configuration and assessment of the GISS ModelE2 contributions to the  
l093 CMIP5 archive, J. Adv. Model. Earth Syst., 6, 141-184, 2014.

l094 Sekhon, R. S., and Srivastava, R.: Doppler radar observations of drop-size distributions in a  
l095 thunderstorm, J. Atmos. Sci., 28, 983-994, 1971.

l096 Shupe, M. D.: A ground-based multisensor cloud phase classifier, Geophys. Res. Lett., 34, 2007.

l097 Tan, I., and Storelvmo, T.: Sensitivity study on the influence of cloud microphysical parameters on  
l098 mixed-phase cloud thermodynamic phase partitioning in CAM5, J. Atmos. Sci., 73, 709-728, 2016.

l099 Tan, I., Storelvmo, T., and Zelinka, M. D.: Observational constraints on mixed-phase clouds imply  
l100 higher climate sensitivity, Science, 352, 224-227, 2016.

l101 Tatarevic, A., and Kollias, P.: User's Guide to Cloud Resolving Model Radar Simulator (CR-SIM),  
l102 McGill University Clouds Research Group, Document available at <http://radarscience.weebly.com/radar-simulators.html>. 2015.

l103

l104 [Winker, D. M.: Accounting for multiple scattering in retrievals from space lidar. Proceedings](#)  
l105 [Volume 5059, 12th International Workshop on Lidar Multiple Scattering](#)  
l106 [Experiments; https://doi.org/10.1117/12.512352, 2003](#)

l107

l108 Yoshida, R., Okamoto, H., Hagihara, Y., and Ishimoto, H.: Global analysis of cloud phase and ice  
l109 crystal orientation from Cloud-Aerosol Lidar and Infrared Pathfinder Satellite Observation (CALIPSO)  
l110 data using attenuated backscattering and depolarization ratio, J. Geophys. Res.: Atmos., 115, 2010.

l111 Zhang, Y., Xie, S., Klein, S. A., Marchand, R., Kollias, P., Clothiaux, E. E., Lin, W., Johnson, K.,  
l112 Swales, D., and Bodas-Salcedo, A.: The ARM Cloud Radar Simulator for Global Climate Models: A New  
l113 Tool for Bridging Field Data and Climate Models, Bull. Amer. Meteorol. Soc., 2017.

l114

l115

l116